



ACADEMIC
PRESS

Available online at www.sciencedirect.com

SCIENCE @ DIRECT®

NeuroImage

NeuroImage 20 (2003) 870–888

www.elsevier.com/locate/ynimg

How to correct susceptibility distortions in spin-echo echo-planar images: application to diffusion tensor imaging

Jesper L.R. Andersson,^{a,*} Stefan Skare,^a and John Ashburner^b

^a Karolinska MR Research Centre, Stockholm, Sweden

^b Wellcome Department of Imaging Neuroscience, London, UK

Received 18 October 2002; revised 28 May 2003; accepted 29 May 2003

Abstract

Diffusion tensor imaging is often performed by acquiring a series of diffusion-weighted spin-echo echo-planar images with different direction diffusion gradients. A problem of echo-planar images is the geometrical distortions that obtain near junctions between tissues of differing magnetic susceptibility. This results in distorted diffusion-tensor maps. To resolve this we suggest acquiring two images for each diffusion gradient; one with bottom-up and one with top-down traversal of k -space in the phase-encode direction. This achieves the simultaneous goals of providing information on the underlying displacement field and intensity maps with adequate spatial sampling density even in distorted areas. The resulting DT maps exhibit considerably higher geometric fidelity, as assessed by comparison to an image volume acquired using a conventional 3D MR technique.

© 2003 Elsevier Inc. All rights reserved.

Introduction

A number of techniques to assess differences in gross anatomy between healthy and diseased subjects based on neuroimaging have recently been proposed (e.g., Ashburner et al., 1998; Ashburner and Friston, 2000, Good et al., 2001) and applied (e.g., Wright et al., 1995; Gaser et al., 1999; May et al., 1999; Maguire et al., 2000). An interesting addition to this arsenal is represented by diffusion tensor imaging (DTI) (Le Bihan et al., 1986; Turner et al., 1990; Basser et al., 1994; Pierpaoli et al., 1996), which may potentially offer information on differences in the hardwiring of corticocortical connections between different groups.

While alternative methods exist (e.g., Gudbjartsson et al., 1996) most DTI is based on spin-echo echo-planar images (EPI) acquired with and without special diffusion gradients that spoil the signal in proportion to local

diffusability of water. A well-known problem with EPI is the geometrical and intensity distortions caused by field imperfections in conjunction with the poor bandwidth in the phase-encode direction. These field imperfections are caused by, among other things, eddy-current-induced global gradients (Jezzard et al., 1998) and susceptibility induced local gradients (Jezzard and Balaban, 1995). We have in previous work dealt with the first of these (Andersson and Skare, 2002) and in the present paper we will address the latter.

We further an idea proposed by Bowtell et al. (1994) which entails collecting two echo-planar images, once traversing k -space bottom-up and once top-down. This results in two images with identical magnitude distortions in opposing directions. These two images, together with a model for the image formation process of spin-echo EPI, allow us to estimate the underlying magnetic field map and undistorted images as they would have looked in a homogeneous field.

In the present paper we:

- (a) present a model for the image formation of spin-echo EPI that allows us to reconstruct a least-squares

* Corresponding author. Karolinska MR Research Center, Karolinska Hospital N-8, 171 76 Stockholm, Sweden. Fax: +46-8-5177-6111.

E-mail address: jesper.andersson@ks.se (J.L.R. Andersson).

estimate of an undistorted image from a displacement field and two distorted images with opposing polarity;

- (b) present a simplified model that allows us to estimate the displacement field from two distorted images within a reasonable execution time;
- (c) demonstrate and validate the method by comparing the estimated displacement field with that obtained by directly measured gradient-echo field maps. We also compare the estimated undistorted spin-echo echo-planar images with conventional T1-weighted 3D images;
- (d) show that with this method we can obtain accurate diffusion-tensor maps with very little distortion.

Theory

Susceptibility induced distortions

For a conventional 2D imaging sequence, if we assume a perfect slice profile, the signal at a given time t can be

expressed as an integration of signal across the locations in that slice,

$$S(t) \propto \iint_{x^* y} \rho(x, y) e^{i\gamma[\Delta B(x,y) + G_f(x,y,t) + G_p(x,y,t)]} dx dy, \quad (1)$$

where γ is the gyromagnetic ratio, G_f and G_p denote the time-integral of the field changes induced by the frequency- and phase-encoding gradients g_f and g_p , respectively, and ΔB denotes field inhomogeneity. Note that we have omitted the effects from transverse relaxation during the readout in Eq. (1). Munger et al. (2000) have formulated (a discrete version of) this such that

$$\underline{\mathbf{s}} = \underline{\mathbf{A}} \underline{\boldsymbol{\rho}}, \quad (2)$$

$m \times 1 \quad m \times n_x n_y \quad n_x n_y \times 1$

where \mathbf{s} is a column vector representation of our signal measured at m time points, $\boldsymbol{\rho}$ is an “image,” the size of $n_x \times n_y$, of our “object” unravelled into a column vector and where \mathbf{A} is

$$\mathbf{A} = \begin{bmatrix} e^{i\gamma[\Delta B_0(x_1,y_1)t_1 + G_f(x_1,y_1,t_1) + G_p(x_1,y_1,t_1)]} & e^{i\gamma[\Delta B_0(x_2,y_1)t_1 + G_f(x_2,y_1,t_1) + G_p(x_2,y_1,t_1)]} & \dots & e^{i\gamma[\Delta B_0(x_{n_x},y_n) t_1 + G_f(x_{n_x},y_n,t_1) + G_p(x_{n_x},y_n,t_1)]} \\ e^{i\gamma[\Delta B_0(x_1,y_1)t_2 + G_f(x_1,y_1,t_2) + G_p(x_1,y_1,t_2)]} & e^{i\gamma[\Delta B_0(x_2,y_1)t_2 + G_f(x_2,y_1,t_2) + G_p(x_2,y_1,t_2)]} & \dots & e^{i\gamma[\Delta B_0(x_{n_x},y_n) t_2 + G_f(x_{n_x},y_n,t_2) + G_p(x_{n_x},y_n,t_2)]} \\ \vdots & \vdots & \ddots & \vdots \\ e^{i\gamma[\Delta B_0(x_1,y_1)t_m + G_f(x_1,y_1,t_m) + G_p(x_1,y_1,t_m)]} & e^{i\gamma[\Delta B_0(x_2,y_1)t_m + G_f(x_2,y_1,t_m) + G_p(x_2,y_1,t_m)]} & \dots & e^{i\gamma[\Delta B_0(x_{n_x},y_n) t_m + G_f(x_{n_x},y_n,t_m) + G_p(x_{n_x},y_n,t_m)]} \end{bmatrix}. \quad (3)$$

However, let us henceforth ignore such things as ramp sampling and assume that $n_x = n_y = n$ and that $m = n^2$. For most MR imaging sequences (e.g., blipped trapezoidal EPI) G_f and G_p are chosen such that the matrix \mathbf{A} (assuming $\Delta B_0 \equiv 0$) implements the discrete 2D Fourier transform.

Let us denote a matrix similar to \mathbf{A} but with zero ΔB_0 for all voxels by \mathbf{F} . There is then a formulation for the mapping between the “true object” space and the EPI image space given by

$$\underline{\mathbf{f}} = \underline{\mathbf{F}}^H \underline{\mathbf{A}} \underline{\boldsymbol{\rho}} = \underline{\mathbf{K}} \underline{\boldsymbol{\rho}}. \quad (4)$$

$n^2 \times 1 \quad n^2 \times n^2 \quad n^2 \times n^2 \quad n^2 \times 1 \quad n^2 \times n^2 \quad n^2 \times 1$

The disadvantage of Eq. (4) is the sheer size of the matrix \mathbf{K} that renders it impractical to use for image restoration. However, if we let the t_i used to multiply ΔB_0 by in Eq. (3) increase only in discrete steps for each phase-encode step (i.e., we ignore any susceptibility ef-

fects in the frequency-encode direction) then \mathbf{K} becomes block-diagonal, i.e.,

$$\mathbf{K} = \begin{bmatrix} \underline{\mathbf{K}}_1 & \mathbf{0} & \dots & \mathbf{0} \\ \mathbf{0} & \underline{\mathbf{K}}_2 & \dots & \mathbf{0} \\ \vdots & \vdots & \ddots & \vdots \\ \mathbf{0} & \mathbf{0} & \dots & \underline{\mathbf{K}}_n \end{bmatrix}. \quad (5)$$

$n \times n \quad n \times n \quad n \times n$

This means that the problem has been reduced to a series of manageable, column-wise (in the phase-encode direction) 1D equations. The “true” intensity-profile along a column in the phase-encode direction is then related to the measured profile according to

$$\hat{\boldsymbol{\rho}}_i = \mathbf{K}_i^+ \mathbf{f}_i, \quad (6)$$

where $^+$ denotes inverse or pseudo-inverse depending on

whether \mathbf{K}_i is of full rank, \mathbf{f}_i denotes the i th column of the EPI image, $\hat{\boldsymbol{\rho}}_i$ denotes the estimated true column, and \mathbf{K}_i is given by $\mathbf{K}_i = \mathbf{F}^H \mathbf{A}_i$ where \mathbf{F} is constructed such that the element at its j th row and k th column is given by

$$\mathbf{F}_{jk} = e^{-2\pi\sqrt{-1}\frac{(j-\frac{n}{2}-1)(k-\frac{n}{2}-1)}{n}}, \quad j, k = 1, 2, \dots, n \quad (7)$$

and where the equivalent for \mathbf{A}_i is

$$[\mathbf{A}_i]_{jk} = e^{-2\pi\sqrt{-1}\left(\frac{(j-\frac{n}{2}-1)(k-\frac{n}{2}-1)}{n} + \frac{j}{n}\Delta B_0(x_i, y_k)\right)}, \quad j, k = 1, 2, \dots, n, \quad (8)$$

where ΔB_0 has been scaled by the reciprocal of the bandwidth per voxel in the phase-encode direction to yield a unit of image pixels.

Eq. (6) is what Munger et al. suggest (a related formulation was suggested by Kadah and Hu, 1997) should be used to restore susceptibility degraded EPI images, given knowledge of ΔB_0 .

However, there are areas of the image that are not successfully restored using Eq. (6) and we will now see why and what can be done about it.

On the implementation of \mathbf{K}

Note that \mathbf{K} is a complex matrix and that an intensity profile through an EPI image corresponds to $|\mathbf{K}_i \boldsymbol{\rho}_i|_{\text{abs}}$, i.e., the modulus of the complex vector resulting from multiplying the real object $\boldsymbol{\rho}$ with the complex matrix \mathbf{K} . That means that with this formulation we would need to work with complex image data (\mathbf{f}) in Eq. (6). We think that would limit the practical usefulness of the method and we would prefer to work with modulus images. To achieve this we choose to implement the matrix \mathbf{K} in a slightly different manner. We use a linear interpolation model and geometrical arguments similar to that of Weis and Budinsky (1990) to obtain a matrix \mathbf{K} with one interpolation kernel for each row. The difference between $|\mathbf{K}_i^+ \mathbf{f}_i|_{\text{abs}}$ (where \mathbf{K}_i is created using Eq. (7) and (8)) and $|\mathbf{K}_i^+ \mathbf{f}_i|_{\text{abs}}$ (where \mathbf{K}_i is created using geometry) is one of interpolation model (Fourier vs linear). Hence, \mathbf{K} will hereafter denote a real matrix.

On the existence of \mathbf{K}^{-1}

The matrix \mathbf{K} is simply the mapping from (a column of) the true (pixelised) object to the distorted image (see Fig. 1). Deviations from the identity matrix, i.e., the wiggles on the diagonal band, are indicative of distortions. Any portion of the matrix with several nonzero values on the same row indicates a many-to-one mapping. We cannot reverse that, just as we cannot deduce a sample from its mean. Hence, \mathbf{K} is rank deficient and no unique inverse exists. Using the pseudo-inverse will just yield that the values of the entire

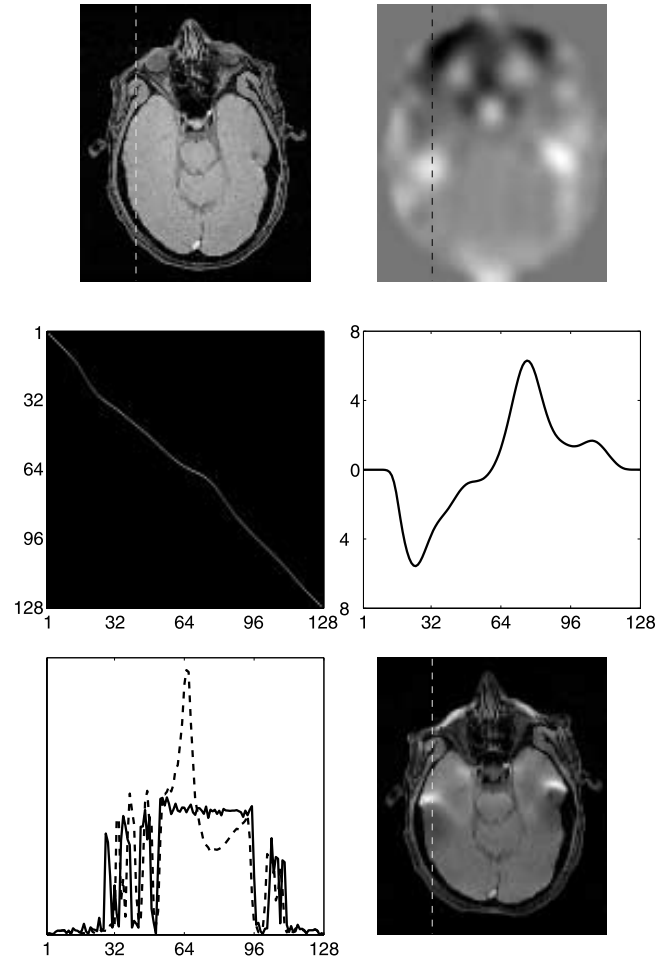


Fig. 1. The upper left panel shows a gradient-echo image through a plane known to be affected by susceptibility problems. The upper right panel shows a field-map through the same plane. The field-map has been scaled using acquisition parameters for a typical 128×128 single-shot EPI image to render it in terms of pixels of displacement. Dark areas indicate a downwards displacement and the bright areas an upwards displacement for an EPI acquisition with positive blips. The middle right panel shows the displacement (in pixels) of each pixel along the line indicated in the upper panels (going from top to bottom). The middle left panel shows the corresponding interpolation matrix (\mathbf{K}) from true to distorted space. The lower left panel shows the intensity profile along that same line (going from top to bottom) for the original image (solid line) and after multiplication with the matrix shown in the middle left (dashed line). The lower right panel shows the resulting “distorted” image after each column has been multiplied with the appurtenant \mathbf{K} matrix. It is interesting to note the quite long stretch of monotonically increasing positive displacements from pixel ~ 30 to ~ 70 which indicates that all these pixels (the entire front bit of the brain along this column) have been compressed. After that, there is a stretch of monotonically decreasing displacements which means that the posterior half has been stretched. A careful study of the top left and lower right panels shows that this is indeed the case.

sample are identical to the mean. Hence, whenever large gradients in the phase-map coincide with nonzero gradients in the intensity map (the image) the problem is poorly solved. The lower right panel of Fig. 1 demonstrates the distortions expected from the displacement field in the upper right panel when acting in the intensity image in the

upper left panel. The hyperintense areas in the distorted image correspond to a stacking of intensity from several voxels in the image in upper right panel to a single (or at least fewer) voxel in the distorted space. It should be clear from this image that it is not possible to accurately reconstruct the intensity from these areas given just the distorted (measured by an EPI sequence) image and knowledge of ΔB_0 .

On the existence of $\begin{bmatrix} \mathbf{K}_+ \\ \mathbf{K}_- \end{bmatrix}^+$

k -space can be traversed from the bottom towards the top (positive blips) or from the top towards the bottom (negative blips). Eq. (7) implicitly assumes top-down sampling in that k increases when going left to right in the matrix \mathbf{F} . A bottom-up sampling would be described by simply traversing k in the reverse order when creating \mathbf{A} and \mathbf{F} . This results in a sign reversal of the effects of ΔB_0 (it would be equivalent to retain the sign of k and sign-reverse ΔB_0) which means that each susceptibility-induced displacement in the top-down image is mirrored by a displacement of identical magnitude but opposite direction in the bottom-up image.

The idea of traversing k -space in opposite directions was originally suggested by Chang and Fitzpatrick (1992) for non-EPI sequences. It was subsequently adapted to EPI (Bowtell et al., 1994) as an alternative to multiple echo times for the assessment of field-maps (Jezzard and Balaban, 1995). We will here show how it can be used to solve the problem of reconstructing the true intensity image from distorted data.

Let us denote, for a given column in the phase-encode direction, the matrix mapping from the true column to that observed with a top-down traversal by \mathbf{K}_- and that for a bottom-up traversal by \mathbf{K}_+ . Note that both are easily created using Eq. (7) and (8) and that their existence is guaranteed by the simple fact that we can observe their effects (by performing the corresponding EPI acquisition). We can now formulate a model for data acquired in both these manners, denoted \mathbf{f}_- and \mathbf{f}_+ , according to

$$\underbrace{\begin{bmatrix} \mathbf{f}_+ \\ \mathbf{f}_- \end{bmatrix}}_{2n \times 1} = \underbrace{\begin{bmatrix} \mathbf{K}_+ \\ \mathbf{K}_- \end{bmatrix}}_{2n \times n} \underbrace{\boldsymbol{\rho}}_{n \times 1}, \quad (9)$$

which is easily solved, in a least squares sense, by

$$\hat{\boldsymbol{\rho}} = \left(\begin{bmatrix} \mathbf{K}_+^T & \mathbf{K}_-^T \\ \mathbf{K}_+^T & \mathbf{K}_-^T \end{bmatrix} \right)^{-1} \begin{bmatrix} \mathbf{K}_+^T \\ \mathbf{K}_-^T \end{bmatrix} \begin{bmatrix} \mathbf{f}_+ \\ \mathbf{f}_- \end{bmatrix}, \quad (10)$$

i.e., by using the generalised inverse of the augmented matrix. There is a matrix-inverse also here, but this time its existence is guaranteed by the specifics of \mathbf{K}_+ and \mathbf{K}_- . Each portion of \mathbf{K}_+ with a less than unity slope of the nonzero band is counteracted by a corresponding band of more than unity slope in \mathbf{K}_- . In other words, each area of \mathbf{f}_+ where voxels have been compressed, and hence are indistinguish-

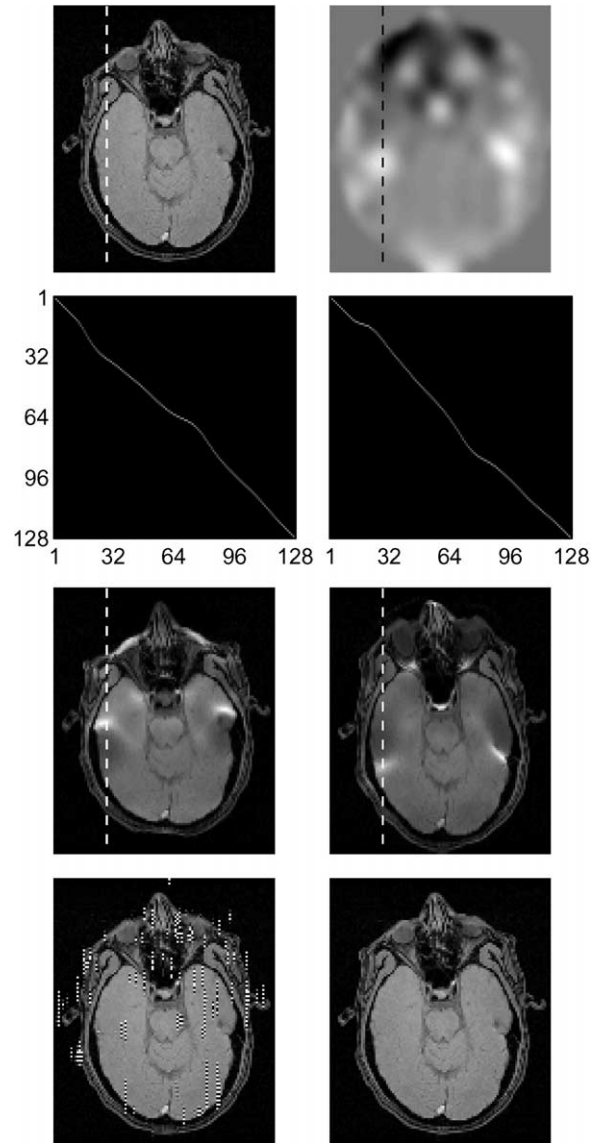


Fig. 2. The upper two panels show a gradient echo image (left) and a field-map at the same location (right). The next two panels show the interpolation matrices for the column indicated by a dashed line in the top two panels for an EPI acquisition with positive blips (\mathbf{K}_+) and negative blips (\mathbf{K}_-). The third row shows the (expected) distorted images acquired with positive (left) and negative (right) phase-encode blips. A low level (standard deviation: 0.1% of average image intensity) of white gaussian noise has been added to the distorted images. This was done to demonstrate the extreme noise sensitivity resulting from using the Moore–Penrose pseudo-inverse of a singular matrix. The lower left panel shows the result when attempting to restore the “true” image using Eq. (6) and the positive blip data alone (third row, left). The obvious ringing artefacts originate from the inversion (Moore–Penrose pseudo-inverse) of a set of fundamentally noninvertible matrices. Less obvious in this figure, but still present, is the total loss of any detail in the areas that were previously compressed (bright in the third row, left). The lower right image has been restored using Eq. (10) and both sets of distorted images and is almost a replica of the original image.

able, corresponds to an area of \mathbf{f}_- where they have been stretched and hence are easily resolved. In Fig. 2 we attempt an intuitive explanation of the concepts in this section.

Hence, given knowledge of ΔB_0 , we suggest acquiring data by traversing k -space twice with different directions in the phase-encode direction and using Eq. (10) to reconstruct the true image. In the next section we will see how these data can be used also for the estimation of $\Delta B_0(x, y, z)$ without the need for any additional measurements.

Estimating $\Delta B_0(x, y, z)$: an image restoration approach

Eq. (9) relates the true intensity profile along an image column to that expected in a bottom-up acquired EPI (denoted \mathbf{f}_+) and a top-down acquired EPI (denoted \mathbf{f}_-) in a least squares sense. From Eq. (10) we can project data back into the distorted spaces, yielding the best model fit to the data given the present model as instantiated by \mathbf{K}_+ and \mathbf{K}_- .

$$\begin{aligned} \begin{bmatrix} \widehat{\mathbf{f}}_+ \\ \widehat{\mathbf{f}}_- \end{bmatrix} &= \begin{bmatrix} \mathbf{K}_+(\mathbf{b}) \\ \mathbf{K}_-(\mathbf{b}) \end{bmatrix} \\ &\times \left(\begin{bmatrix} \mathbf{K}_+^T(\mathbf{b}) & \mathbf{K}_-^T(\mathbf{b}) \end{bmatrix} \begin{bmatrix} \mathbf{K}_+(\mathbf{b}) \\ \mathbf{K}_-(\mathbf{b}) \end{bmatrix} \right)^{-1} \\ &\times \begin{bmatrix} \mathbf{K}_+^T(\mathbf{b}) & \mathbf{K}_-^T(\mathbf{b}) \end{bmatrix} \begin{bmatrix} \mathbf{f}_+ \\ \mathbf{f}_- \end{bmatrix}, \end{aligned} \quad (11)$$

where the displacements have been parameterised by some vector \mathbf{b} . When assuming no displacements (i.e., $\mathbf{b} = 0$), both \mathbf{K}_+ and \mathbf{K}_- are simply the unity matrix and the estimate $\widehat{\boldsymbol{\rho}}$ given by Eq. (10) is the average of \mathbf{f}_+ and \mathbf{f}_- . The ability of \mathbf{b} to explain the observed data can be assessed from the difference between the observed \mathbf{f}_+ and \mathbf{f}_- and the best model fit $\widehat{\mathbf{f}}_+$ and $\widehat{\mathbf{f}}_-$, i.e., by

$$\begin{bmatrix} \widehat{\mathbf{e}}_+ \\ \widehat{\mathbf{e}}_- \end{bmatrix} = \underbrace{\mathbf{R}(\mathbf{b})}_{2n \times 2n} \begin{bmatrix} \mathbf{f}_+ \\ \mathbf{f}_- \end{bmatrix}, \quad (12)$$

where $\mathbf{R}(\mathbf{b})$ is

$$\begin{aligned} \mathbf{R}(\mathbf{b}) &= \mathbf{I} - \begin{bmatrix} \mathbf{K}_+(\mathbf{b}) \\ \mathbf{K}_-(\mathbf{b}) \end{bmatrix} \\ &\times \underbrace{\left(\begin{bmatrix} \mathbf{K}_+^T(\mathbf{b}) & \mathbf{K}_-^T(\mathbf{b}) \end{bmatrix} \begin{bmatrix} \mathbf{K}_+(\mathbf{b}) \\ \mathbf{K}_-(\mathbf{b}) \end{bmatrix} \right)^{-1}}_{n \times n} \\ &\times \underbrace{\begin{bmatrix} \mathbf{K}_+^T(\mathbf{b}) & \mathbf{K}_-^T(\mathbf{b}) \end{bmatrix}}_{n \times 2n}, \end{aligned} \quad (13)$$

i.e., the residual forming matrix for the image restoration model for displacements determined by \mathbf{b} .

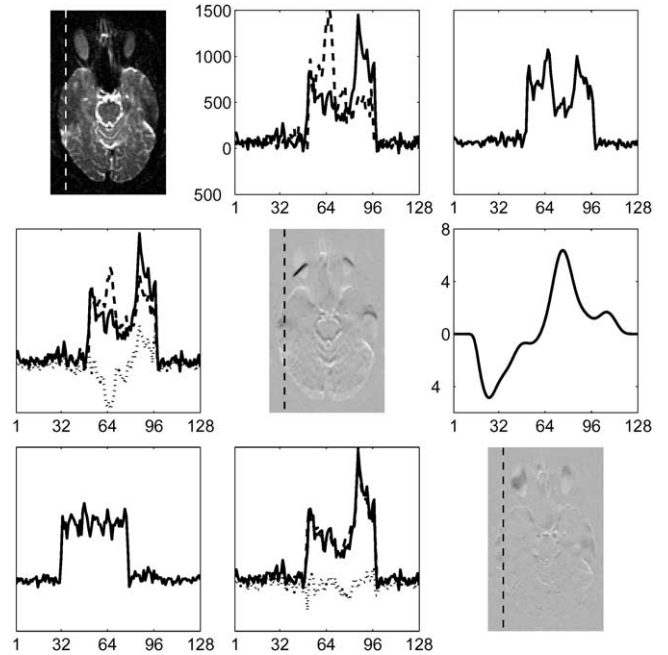


Fig. 3. The top left panel shows an SE-EPI image acquired with negative phase-encode blips. The top middle panel shows the intensity profiles (for the column indicated in the previous panel) for positive (solid line) and negative phase-encode blips (dashed line). Note that these correspond to the vectors \mathbf{f}_+ and \mathbf{f}_- in Eq. (9) and (10). The top right panel shows $\widehat{\boldsymbol{\rho}}$ estimated using Eq. (10) assuming a homogeneous field (i.e., $\mathbf{K}_+ = \mathbf{K}_- = \mathbf{I}$). In the middle left panel the solid line is the observed intensity profile with negative phase-encode blips (\mathbf{f}_-) and the dashed line is the intensity profile predicted by the model (i.e., $\widehat{\mathbf{f}}_-$ from Eq. (11)) when assuming a homogeneous field. The dotted line finally corresponds to the difference between the observed and predicted intensity profiles, i.e., $\widehat{\mathbf{e}}_-$ from Eq. (12). The middle middle panel shows $\widehat{\mathbf{e}}_-$ for every column stacked to form an error image. It can be seen from this image that there is some considerable mismatch between the observations and the model predictions and hence that the assumption of a homogeneous field was not tenable. If instead we “assume” another displacement field, for which the pertinent column is shown in the middle right panel, the estimated intensity profile $\widehat{\boldsymbol{\rho}}$ is given by the lower left panel. This results in the \mathbf{f}_- , $\widehat{\mathbf{f}}_+$, and $\widehat{\mathbf{e}}_-$ (solid, dashed, and dotted lines, respectively) shown in the lower middle panel. The lower right panel finally shows the error image for this “other” field, indicating a much better correspondence between data and model.

Hence, we suggest that the displacements (\mathbf{b}) that best explain the observed data are those given by

$$\min_{\arg=\mathbf{b}} O(\mathbf{b}) = \left(\sum_{c=1}^m [\mathbf{f}_{c+}^T \quad \mathbf{f}_{c-}^T] \mathbf{R}_c(\mathbf{b}) \begin{bmatrix} \mathbf{f}_{c+} \\ \mathbf{f}_{c-} \end{bmatrix} \right), \quad (14)$$

i.e., that which minimises the squared deviation between the observed data and the model fit across all (in the entire volume) phase-encode columns c .

Fig. 3 offers an intuitive explanation of the concepts of this section.

Estimating $\Delta B_0(x, y, z)$: modelling the field

Let us denote the true space as $\mathbf{x} = [x, y, z]^T$, the space of a bottom-up acquired EPI image as $\mathbf{x}_+ = [x_+, y_+, z_+]^T$, and that of a top-down EPI by $\mathbf{x}_- = [x_-, y_-, z_-]^T$. Furthermore, let us denote the mapping $\mathbf{x} \rightarrow \mathbf{x}_+$ by T_+ and the mapping $\mathbf{x} \rightarrow \mathbf{x}_-$ by T_- . Both T_+ and T_- are uniquely determined by a displacement field $d(\mathbf{x}) \propto \Delta B_0(\mathbf{x})$ where $\mathbf{x}_+ = T_+(\mathbf{x}) = [x, y + d(\mathbf{x}), z]^T$ and $\mathbf{x}_- = T_-(\mathbf{x}) = [x, y - d(\mathbf{x}), z]^T$. The process of finding the $\Delta B_0(\mathbf{x})$ field that results in two observed data sets $f_+(\mathbf{x}_+)$ and $f_-(\mathbf{x}_-)$ can be thought of as finding the displacement field $d(\mathbf{x})$ that fulfills

$$\left| \frac{\partial(\mathbf{x}_+)}{\partial(\mathbf{x})} \right|_{\mathbf{x}_+} f_+(\mathbf{x}_+) = \left| \frac{\partial(\mathbf{x}_-)}{\partial(\mathbf{x})} \right|_{\mathbf{x}_-} f_-(\mathbf{x}_-) \quad (15)$$

for every \mathbf{x} (for an explanation of relevant concepts see Chap. 5 of the excellent Marsden and Tromba, 1981).

Previous implementations of the “dual phase-blip” method (Bowtell et al. (1994)) have addressed a fundamentally three-dimensional estimation problem as if it was a large set of independent one-dimensional problems. Hence, the 1D displacement “field” along one column has no connection to those of the surrounding columns. This will make the problem poorly conditioned, since fewer data are used for the determination of each parameter, and results in nonsensical “striped” $\Delta B_0(\mathbf{x})$ fields.

Spatial continuity of warps can be ensured by modelling them as linear combinations of basis warps (e.g., Thurfjell et al., 1993; Woods et al., 1998; Ashburner and Friston, 1999; Kybic et al., 2000; Studholme et al., 2000; Andersson et al., 2001). In this paper we will model the $\Delta B_0(\mathbf{x})$ field as a linear combination of basis warps consisting of a truncated 3D cosine transform (Jain, 1989; Ashburner and Friston, 1999). We will denote this as $\Delta B_0(\mathbf{x}, \mathbf{b})$ where \mathbf{b} is the vector of weights of the basis warps. Similarly we will use the notation $d(\mathbf{x}, \mathbf{b})$. In contrast to previous implementations of the Chang and Fitzpatrick idea (1992), this will result in a smooth and continuous estimate of the displacement field. We present Fig. 4 as a demonstration of this.

Estimating $\Delta B_0(x, y, z)$: an approximate approach

We shall precede the results and disclose that Eq. (14) is not practical to use for the estimation of \mathbf{b} . The problem originates from viewing the matrix \mathbf{R} , rather than the data \mathbf{f} as is common practice (e.g., Ashburner et al., 1999), as a function of \mathbf{b} . This renders the estimation of the partial derivatives of $O(\mathbf{b})$ with respect to \mathbf{b} difficult, which means that one has to resort to very slow search methods (e.g., Powell, 1964).

We will therefore present a method to estimate the displacement field $d(\mathbf{x}, \mathbf{b})$ that is based on an approximate

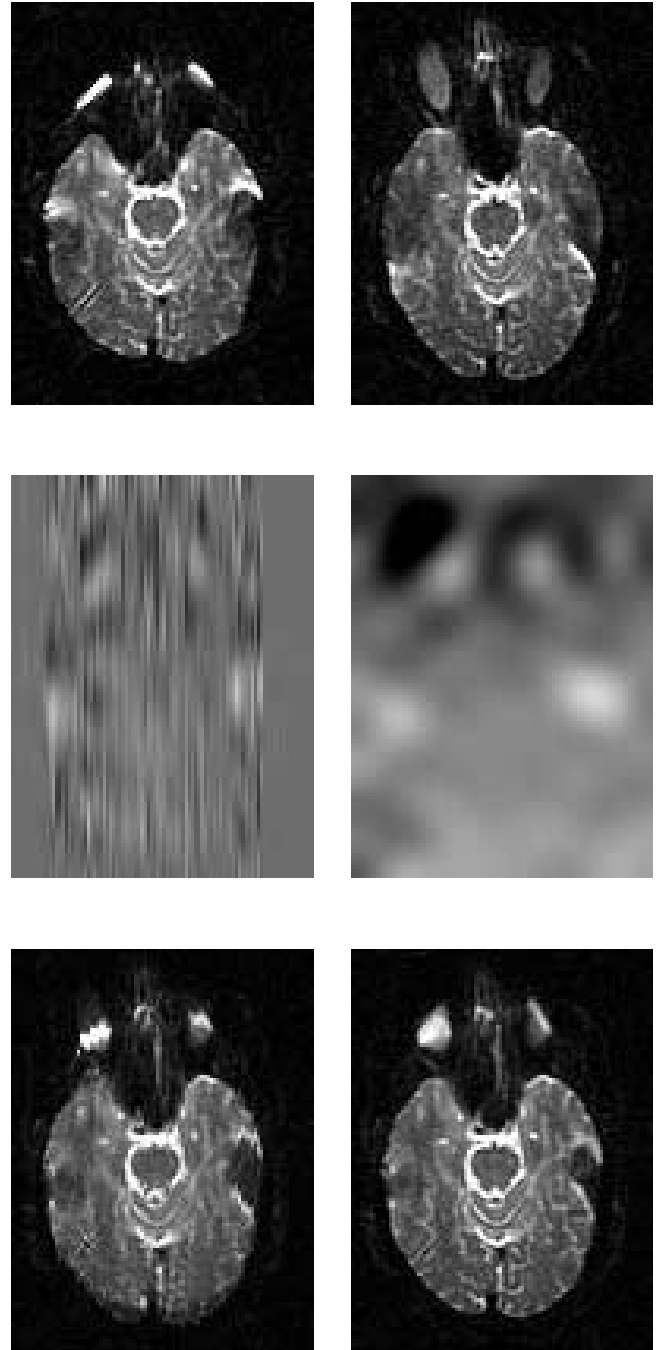


Fig. 4. The top panels show SE-EPI images acquired with positive (left) and negative (right) phase-encode blips. Note the high degree of agreement with the simulated data shown in the third row of Fig. 2. The second row shows the estimated displacement fields using a 1D- (left) and a 2D-model (right). Both fields were estimated using Eq. (14) (i.e., using the exact model), although in the 1D case there were of course no summations across columns. For the 1D case the field along each of the 96 columns were modelled as a linear combination of the 12 first basis functions of the DCT set, yielding a total of 1152 unknowns. The 2D field was modelled as the 9×12 first basis functions of the 2D DCT set. The bottom row shows the restored images (using both blip directions and Eq. (10)) based on the field from the 1D model (left) and that from the 2D model (right).

model, one that is computationally more tractable. The estimated field will then be used to reconstruct the intensity map using the exact model. In addition the ability of the approximate model to find the true displacement field will be gauged by comparison to the exact model.

The next approximation we will use is based on the Jacobian modulation indicated in Eq. (15). Specifically we will assume that

$$f_+(\mathbf{x} - [0 \quad d(\mathbf{x}, \mathbf{b}) \quad 0]^T) \left(1 - \frac{\partial d}{\partial y} \Big|_{\mathbf{x}} \right) \approx f_-(\mathbf{x} + [0 \quad d(\mathbf{x}, \mathbf{b}) \quad 0]^T) \left(1 + \frac{\partial d}{\partial y} \Big|_{\mathbf{x}} \right), \quad (16)$$

which makes

$$\sum_{\mathbf{x} \in V} \left(f_+(\mathbf{x} - [0 \quad d(\mathbf{x}, \mathbf{b}) \quad 0]^T) \left(1 - \frac{\partial d}{\partial y} \Big|_{\mathbf{x}} \right) - f_-(\mathbf{x} + [0 \quad d(\mathbf{x}, \mathbf{b}) \quad 0]^T) \left(1 + \frac{\partial d}{\partial y} \Big|_{\mathbf{x}} \right) \right)^2, \quad (17)$$

i.e., the sum of squared differences between the resampled and modulated top-down and bottom-up image volumes, a suitable choice of cost function.

Furthermore, we denote our basis set as $\mathbf{B}(\mathbf{x}) = \mathbf{B}_z(z) \otimes \mathbf{B}_y(y) \otimes \mathbf{B}_x(x)$ where n_z , n_y , and n_x are the size of the image volume in the z -, y -, and x -directions, respectively, and where m_z , m_y , and m_x denote the number of basis functions for each direction. This allows us to express the partial derivatives of the two image volumes with respect to \mathbf{b} as

$$\frac{d\mathbf{f}_+}{d\mathbf{b}} = - \underbrace{\text{diag} \left(\frac{\partial \mathbf{f}_+}{\partial y} \right)}_{n \times n} \underbrace{\mathbf{B}}_{n \times m} - \underbrace{\text{diag}(\mathbf{f}_+)}_{n \times n} \underbrace{\frac{\partial \mathbf{B}}{\partial y}}_{n \times m} \quad (18)$$

and

$$\frac{d\mathbf{f}_-}{d\mathbf{b}} = \underbrace{\text{diag} \left(\frac{\partial \mathbf{f}_-}{\partial y} \right)}_{n \times n} \underbrace{\mathbf{B}}_{n \times m} + \underbrace{\text{diag}(\mathbf{f}_-)}_{n \times n} \underbrace{\frac{\partial \mathbf{B}}{\partial y}}_{n \times m}, \quad (19)$$

where

$$\frac{\partial \mathbf{B}}{\partial y} = \underbrace{\mathbf{B}_z}_{n_z \times m_z} \otimes \underbrace{\frac{\partial \mathbf{B}_y}{\partial y}}_{n_y \times m_y} \otimes \underbrace{\mathbf{B}_x}_{n_x \times m_x}. \quad (20)$$

This allows us, using ideas from Ashburner and Friston

(1999) and Andersson and Skare (2002), to formulate an estimation model for \mathbf{b}

$$\underbrace{\mathbf{b}_i}_{m \times 1} = \underbrace{\mathbf{b}_{i-1}}_{m \times 1} + \left(\underbrace{\left[\left(\frac{d\mathbf{f}_+}{d\mathbf{b}} \right)^T \quad \left(\frac{d\mathbf{f}_-}{d\mathbf{b}} \right)^T \right]}_{m \times 2n} \underbrace{\begin{bmatrix} \mathbf{I} & -\mathbf{I} \\ -\mathbf{I} & \mathbf{I} \end{bmatrix}}_{2n \times 2n} \underbrace{\begin{bmatrix} \frac{d\mathbf{f}_+}{d\mathbf{b}} \\ \frac{d\mathbf{f}_-}{d\mathbf{b}} \end{bmatrix}}_{2n \times m} \right)^{-1} \times \left(\underbrace{\left[\left(\frac{d\mathbf{f}_+}{d\mathbf{b}} \right)^T \quad \left(\frac{d\mathbf{f}_-}{d\mathbf{b}} \right)^T \right]}_{m \times 2n} \underbrace{\begin{bmatrix} \mathbf{I} & -\mathbf{I} \\ -\mathbf{I} & \mathbf{I} \end{bmatrix}}_{2n \times 2n} \underbrace{\begin{bmatrix} \mathbf{f}_+ \\ \mathbf{f}_- \end{bmatrix}}_{2n \times 1} \right) \quad (21)$$

for iterations $i = 1, 2, \dots$, where m now denotes the number of spatial basis functions used to model $d(\mathbf{x}, \mathbf{b})$ and n is the total number of voxels in the 3D image volume.

We leave a detailed derivation of Eq. (21) to the Appendix and just state that this can be calculated in a rapid manner, capitalising on the separability of the basis set as has been described previously (Ashburner and Friston, 1999). As will be seen later in the paper, we need to model the displacement field with a large number of basis functions so a direct calculation of Eq. (21) would literally be impossible.

Estimating $\Delta B_0(x, y, z)$: including subject movement and regularisation

Eq. (21) above is based on the assumption that any difference between \mathbf{f}_+ and \mathbf{f}_- can be attributed to susceptibility effects. Unfortunately, there are at least two other sources that can contribute to this difference. One has to do with the handling of the centre frequency in the reconstruction software, which may cause in-plane translations between the two acquisitions. The other is subject movement. Movements between the acquisition of \mathbf{f}_+ and \mathbf{f}_- will cause differences between them and severely disrupt any attempt at estimating the susceptibility-induced displacement field. Furthermore, as can be appreciated from the top panels of Fig. 4, any attempt at realigning them prior to the estimation is likely to fail.

Our solution is to include a rigid-body movement into the model, simultaneously estimating any position differences between the two acquisitions and the displacement field.

Additionally, in parts of the image volume where the signal is close to zero (i.e., in the air outside the object) there is little information to guide the estimation of warps, and pretty much any set of warps will yield an equally “good” solution. To prevent excessive warping in these areas we have included also a regularisation term based on the sum of squared first derivatives of the warping field.

The full derivation of how to include movement effects

is also left for the Appendix. For the inclusion of the regularisation term we simply refer to Ashburner and Friston (1999).

Special considerations for diffusion tensor imaging

A diffusion tensor image is formed by combining information from a “regular” T2-weighted spin-echo echo-planar image with information from (six or more) diffusion-weighted images with diffusion gradients applied in different directions. Multiple acquisitions are often performed for each direction to improve the signal-to-noise ratio. Hence, in contrast to, e.g., in fMRI, we are imaging a parameter that is expected to be stationary in time. It is therefore particularly suited for the method we suggest in the present paper since the underlying assumption

that the signal in the two acquisitions differs only with respect to the effects of susceptibility induced field inhomogeneities is fulfilled. We suggest collecting two images, with different sign phase-encode blips, for each diffusion direction, as well as for the T2-weighted reference scan. This means, given knowledge about the displacement field, that a pristine image, with susceptibility-induced effects removed, can be restored for each diffusion direction. These can subsequently be combined to yield a distortion-free diffusion tensor map.

In addition, each pair of images contributes information about the displacement field and can be used in Eq. (21) for its estimation. This is done by augmenting the data vectors, the derivative matrices, and the residual-forming matrix to reflect all the pairs in the set.

$$\begin{aligned}
 \underbrace{\mathbf{b} - \mathbf{b}_0}_{m \times 1} &= \left(\underbrace{\left[\left(\frac{d\mathbf{f}_1}{d\mathbf{b}} \right)^T \quad \left(\frac{d\mathbf{f}_2}{d\mathbf{b}} \right)^T \quad \dots \quad \left(\frac{d\mathbf{f}_l}{d\mathbf{b}} \right)^T \right]}_{m \times 2ln} \underbrace{\begin{bmatrix} \mathbf{R} & \mathbf{0} & \dots & \mathbf{0} \\ \mathbf{0} & \mathbf{R} & \dots & \mathbf{0} \\ \vdots & \vdots & \ddots & \vdots \\ \mathbf{0} & \mathbf{0} & \dots & \mathbf{R} \end{bmatrix}}_{2ln \times 2ln} \underbrace{\begin{bmatrix} \frac{d\mathbf{f}_1}{d\mathbf{b}} \\ \frac{d\mathbf{f}_2}{d\mathbf{b}} \\ \vdots \\ \frac{d\mathbf{f}_l}{d\mathbf{b}} \end{bmatrix}}_{2ln \times m} \right)^{-1} \\
 &\times \underbrace{\left[\left(\frac{d\mathbf{f}_1}{d\mathbf{b}} \right)^T \quad \left(\frac{d\mathbf{f}_2}{d\mathbf{b}} \right)^T \quad \dots \quad \left(\frac{d\mathbf{f}_l}{d\mathbf{b}} \right)^T \right]}_{m \times 2ln} \underbrace{\begin{bmatrix} \mathbf{R} & \mathbf{0} & \dots & \mathbf{0} \\ \mathbf{0} & \mathbf{R} & \dots & \mathbf{0} \\ \vdots & \vdots & \ddots & \vdots \\ \mathbf{0} & \mathbf{0} & \dots & \mathbf{R} \end{bmatrix}}_{2ln \times 2ln} \underbrace{\begin{bmatrix} \mathbf{f}_1 \\ \mathbf{f}_2 \\ \vdots \\ \mathbf{f}_l \end{bmatrix}}_{2ln \times 1}, \quad (22)
 \end{aligned}$$

where

$$\frac{d\mathbf{f}_i}{d\mathbf{b}} = \underbrace{\begin{bmatrix} \frac{d\mathbf{f}_{i+}}{d\mathbf{b}} \\ \frac{d\mathbf{f}_{i-}}{d\mathbf{b}} \end{bmatrix}}_{2n \times m}, \quad (23)$$

$$\mathbf{R} = \underbrace{\begin{bmatrix} \mathbf{I} & -\mathbf{I} \\ -\mathbf{I} & \mathbf{I} \end{bmatrix}}_{2n \times 2n}, \quad (24)$$

and

$$\mathbf{f}_i = \underbrace{\begin{bmatrix} \mathbf{f}_{i+} \\ \mathbf{f}_{i-} \end{bmatrix}}_{2n \times 1} \quad (25)$$

and where l is the number of different acquisitions (i.e., the number of diffusion directions plus the unweighted acquisition).

Experiments and implementation

Implementation

The method outlined above was implemented in Matlab (Mathworks, Natick, MA) on a Linux 500-MHz Pentium III PC with 1 GB of RAM. Any number of pairs of images (as outlined in Eq. (22) to (25)) could be entered and used for the determination of the displacement field. An optional number of basis functions could be used to model the displacement field, although in practice it was limited to ~4000 by the RAM requirements. Subject movement pa-

rameters could be included in or excluded from the model. It was assumed that all images in a “set” (i.e., all images acquired with the same phase-encode blip direction) were in the same space (with respect to position and eddy-current induced distortions). Hence, a single set of movement parameters was estimated. A “plastic” regularisation model based on the zeroth- to fourth- (optional) order derivative of the displacements was implemented. A first-order model was used for all calculations in the present paper. Preprocessing of data consisted of Gaussian smoothing (with an arbitrary FWHM) and global intensity normalisation (to compensate for possible differences in gain settings between the two acquisitions).

When the displacement field had been determined undistorted images were reconstructed using the image restoration approach (Eq. (10)) with optional inclusion of a regularisation (first derivative) term for high-noise data. Creation of the \mathbf{K} matrices used for the restoration was optionally according to Eq. (7) and (8) (for use when complex image data are available) or using geometry (Weis and Budinsky, 1990).

Diffusion weighted EPI

Scanning was performed on a 1.5-T GE Signa (GE, Milwaukee, WI) whole body scanner equipped with 22 mT/m gradients. A diffusion-weighted (with a b -value of 1000 s/mm^2) single-shot spin-echo EPI sequence was used. A total of 4 unweighted and 30 isotropic (Jones et al., 1999; Skare et al., 2000) diffusion weighted acquisitions was performed for each blip direction. Acquisition parameters were TE 95 ms, FOV 240 mm, matrix size 128×128 , and slice thickness 3 mm. Peripheral pulse gating (Skare and Andersson, 2001) was employed, collecting two planes per heart beat, yielding an effective TR in the order of $\sim 15 \text{ s}$. Scanning was centred on the caudal parts of the brain including the orbitofrontal cortex, the temporal lobes, and the brain stem, all areas known to be affected by susceptibility artefacts.

Slight modifications of the vendor-supplied pulse sequence and reconstruction program were necessary to enable acquisition and reconstruction of sign-reversed phase-encode blip data.

Eddy-current induced distortions and subject movements within a set of diffusion weighted images were corrected as previously described (Andersson and Skare, 2002) and coregistration of T2- and diffusion-weighted images was performed using mutual information (Maes et al., 1997).

Acquisition and calculation of phase-maps

Gradient-echo images with different echo times were acquired in the same session as the EPI images (above) and with the exact same slice positions and thickness. Acquisition parameters were TR 800 ms, flip-angle 30° , TE 8.4, 12.6, and 16.8 ms, matrix size 256×256 , FOV 240 mm, and slice thickness 3 mm. Images were reconstructed into real and imag-

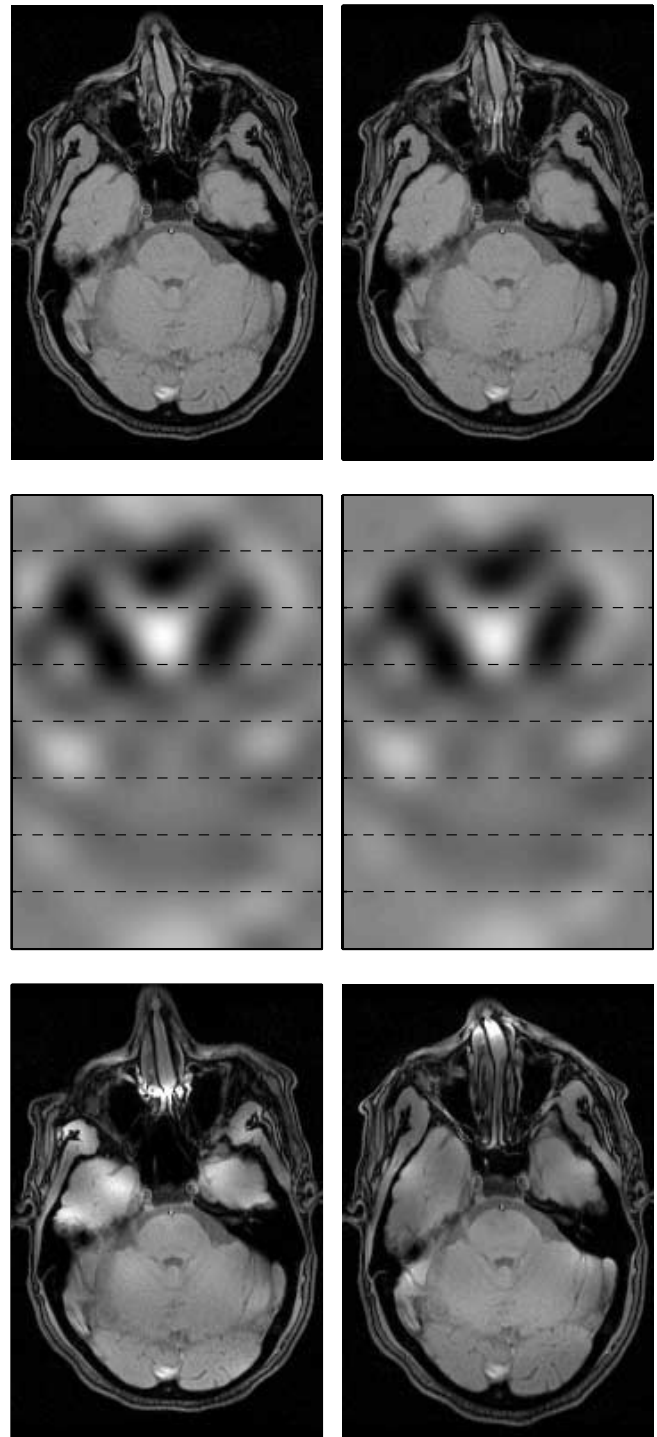


Fig. 5. The top panels show one slice of an “undistorted” gradient-echo image volume (left) and an image that has been restored based on a field estimated using the approximate method (as defined by Eq. (18) to (21)) (right). The second row shows the “true” displacement field (left) that was used to create the two simulated bottom-up and top-down images (third row). The right panel of the second row shows the displacement field estimated from the two simulated images using the approximate method.

inary parts and maps of the regression on the phase-differences between the acquisitions were calculated. An estimate of variance of the phase-difference estimate was calculated for each

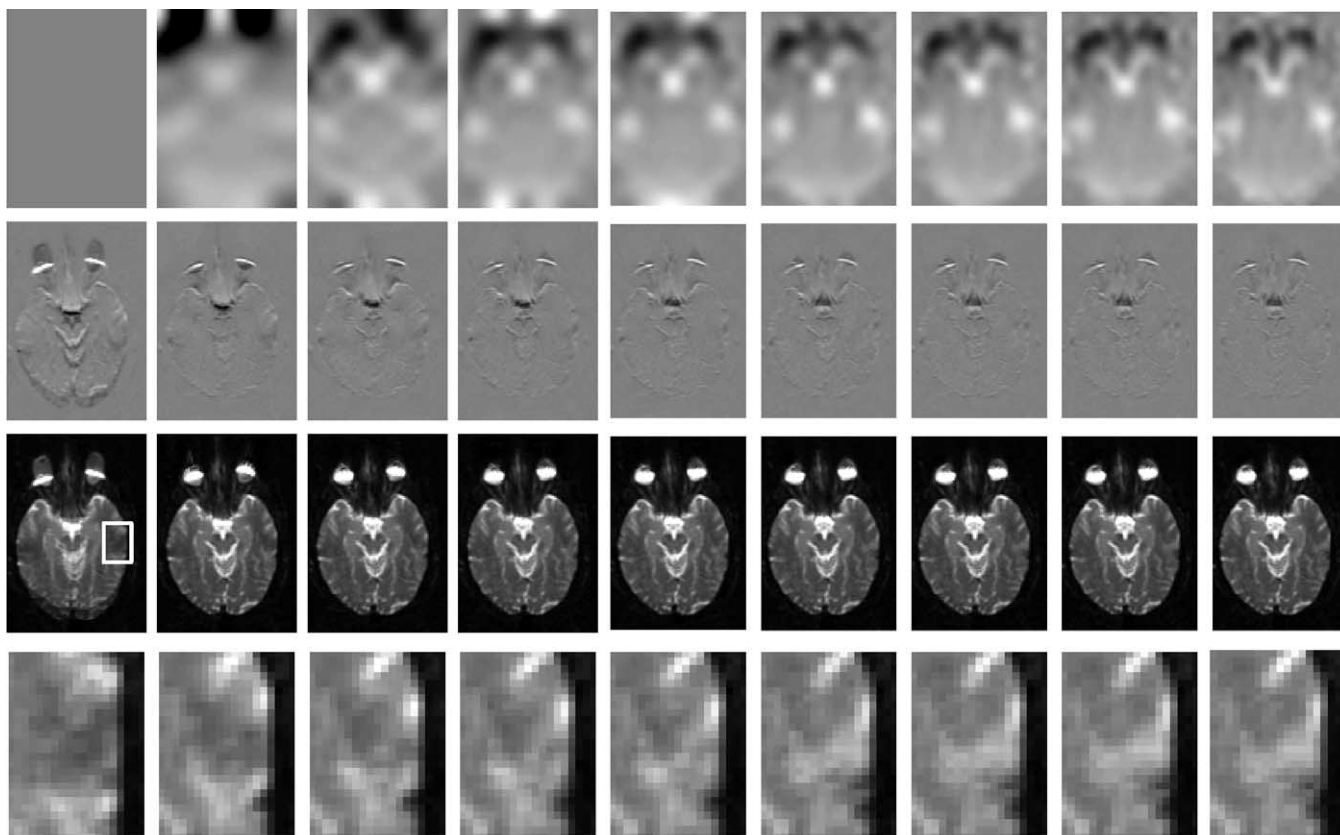


Fig. 6. Rows show, from top to bottom, estimated field, resulting error image, restored image, and zoomed part of restored image. Columns correspond to, from left to right, $0 \times 0 \times 0$ (i.e., homogeneous field), $8 \times 8 \times 3$, $10 \times 10 \times 4$, $12 \times 12 \times 5$, $14 \times 14 \times 5$, $16 \times 16 \times 6$, $18 \times 18 \times 7$, $20 \times 20 \times 7$, and $22 \times 22 \times 8$ basis functions, respectively. The square in the left panel of the third row indicates the area that has been blown up for the bottom row. Note in the bottom row how the sulcus starts out as two distinct hyperintense areas that move towards each other as distortions are modelled with a higher degree of detail until at about $18 \times 18 \times 7$ basis functions they merge (correctly) into one sulcus.

voxel and a seed was placed in a central low-variance voxel. A fully 3D watershed algorithm (using the variance of the phase estimate as the “water level”) was used to direct the evolution of the phase-unwrapping from low- to high-variance areas (somewhat similar to Cusack and Papadakis, 2002). The unwrapped phase-maps were regularised (Jenkinson, 2001) by a weighted (by variance) fit to a 3D cosine-basis set in a manner similar to that of Hutton et al. (2002). The unwrapped, regularised phase-maps were scaled to pixel displacement maps using echo-time difference from the GRE acquisition and echo-readout time from the EPI acquisitions. In addition, unwrapping was compared to that using a completely independent method (Jenkinson, 2003) to ensure that there were no wrapping errors.

Conventional 3D MR data

In order to obtain an anatomical reference a T1-weighted 3D-SPGR sequence with imaging parameters TR 24 ms, TE 6 ms, 35° flip-angle, and a $256 \times 256 \times 124$ matrix with $0.9 \times 0.9 \times 1.5$ mm resolution was used. This scan was performed on a separate occasion.

Analysis

Assessing the accuracy of the approximate model

A crucial question is whether the $d(\mathbf{x}|\mathbf{b})$ that we estimate using the approximate model is a decent likeness of the underlying $\Delta B_0(\mathbf{x})$ field. In order to assess this we used Eq. (9), an experimentally determined (from the from dual-blip EPI images) $\Delta B_0(\mathbf{x})$ field, and undistorted images (gradient-echo again) to create “synthetically” distorted bottom-up and top-down acquired “EPI” images. These images were used to estimate the displacement field by means of Eq. (21) and to restore an undistorted image using the estimated field and Eq. (10). This was performed with and without white noise added to the distorted images.

Assessment of the spatial scale of the distortions

We wanted to determine the number of spatial basis functions necessary to model the observed distortions. Using only the T2-weighted reference images from the EPI data set and Eq. (21) we estimated the field $d(\mathbf{x}|\mathbf{b})$ using

[8 8 3], [10 10 4], [12 12 5], [14 14 5], [16 16 6], [18 18 7], [20 20 7], and [22 22 8] basis functions. These all correspond to roughly the same number of basis functions per distance in the three directions. The resulting fields were visually inspected, as was the restored image associated with each field. The values of both the exact objective-function (Eq. (14)) and the approximate objective function (Eq. (17)) on convergence were recorded for each field.

Sensitivity of estimated field with respect to data

If our model is correct, the estimated field should be independent of the specific information content of the data. For example, if we use Eq. (22), $l = 1$, and use the T2-weighted reference images we would expect to find the same field as if we used an image diffusion weighted in the [1 0 0] direction or in the [0 1 0] or if we used $l = 3$ and all three image pairs. To verify this we estimated displacement fields using Eq. (22), $l = 1$, a T2-weighted image pair, and two diffusion-weighted pairs with near orthogonal diffusion gradients. In addition, we estimated the field using all three pairs. We used [18 18 7] spatial basis functions throughout.

Comparison to dual-echo phase mapping

Displacement maps and restored images estimated using our method were compared to those obtained from the phase measurements.

Visual assessment of registration accuracy

Distorted (\mathbf{f}_+ or \mathbf{f}_-) and undistorted ($\hat{\mathbf{p}}$, estimated from Eq. (22) and (10)) EPI images were coregistered to the conventional T1-weighted scan using mutual information as implemented in SPM. Points of large curvature (e.g., the fundi of sulci) were manually identified and marked in the conventional scan and transferred to the EPI images. Visual inspection was used to assess the correspondence of the marks in the anatomical and the EPI images.

Generation of distortion-free diffusion tensor maps

The entire set of EPI images (5 T₂-weighted and 30 diffusion-weighted) was employed to assess the displacement field using Eq. (22). An undistorted image was created using Eq. (10) for each pair of reference or diffusion-weighted images. These undistorted images were used to estimate tensor-component images from which maps of mean diffusion and anisotropy were calculated. In addition, the same maps were calculated separately from the top down and bottom up (to serve as an example of typical distorted maps). The maps based on the corrected and uncorrected EPI data were coregistered to the conventional images and visual inspection was used to compare them.

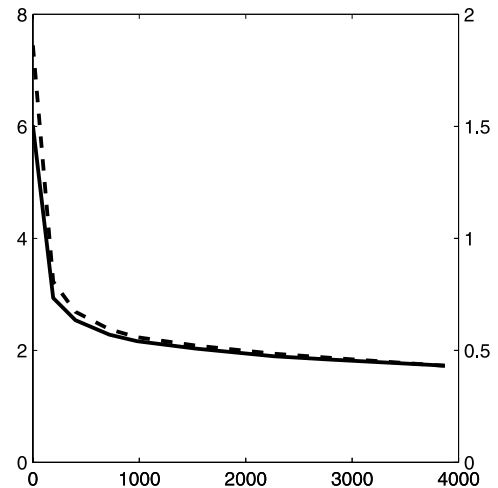


Fig. 7. The solid and dashed lines demonstrate the value of the exact (as given by Eq. (14)) and the approximate (as given by Eq. (17)) cost function, respectively, as a function of the number of basis functions used to model the field.

Results

Assessing the accuracy of the approximate model

An example of images that have been “synthetically” distorted using the exact method (Eq. (9)) to mimic top-down and bottom-up acquired EPI images is shown in the lower row of Fig. 5. The displacement field estimated from these, using the approximate model (Eq. 21), is shown in the middle right panel and demonstrates a high level of similarity to the true field (middle left panel). The resulting restored image in the upper right panel is virtually indistinguishable from the true image in the upper left panel.

Assessment of the spatial scale of the distortions

A cursory examination of the error-maps ($\hat{\mathbf{e}}_-$) in the second row and the restored images in the third row of Fig. 6 may indicate that already a limited number of basis functions (e.g., $12 \times 12 \times 5$ as in the third column) would be sufficient. However, careful scrutiny (as that offered by the blow-up in the fourth row) shows that for the problematic areas (areas with large y -gradients of the susceptibility-induced field) results keep improving all the way up to the maximum number of basis functions permissible by the amount of RAM ($22 \times 22 \times 8$). The same conclusion can be drawn from Fig. 7 where it is shown that the “error” assessed using either the exact (Eq. (14)) or the approximate method is still decreasing as a function number of basis functions.

Furthermore, the close correspondence between the two error terms demonstrated in Fig. 7 lends additional support to using the approximate method for estimation of the field.

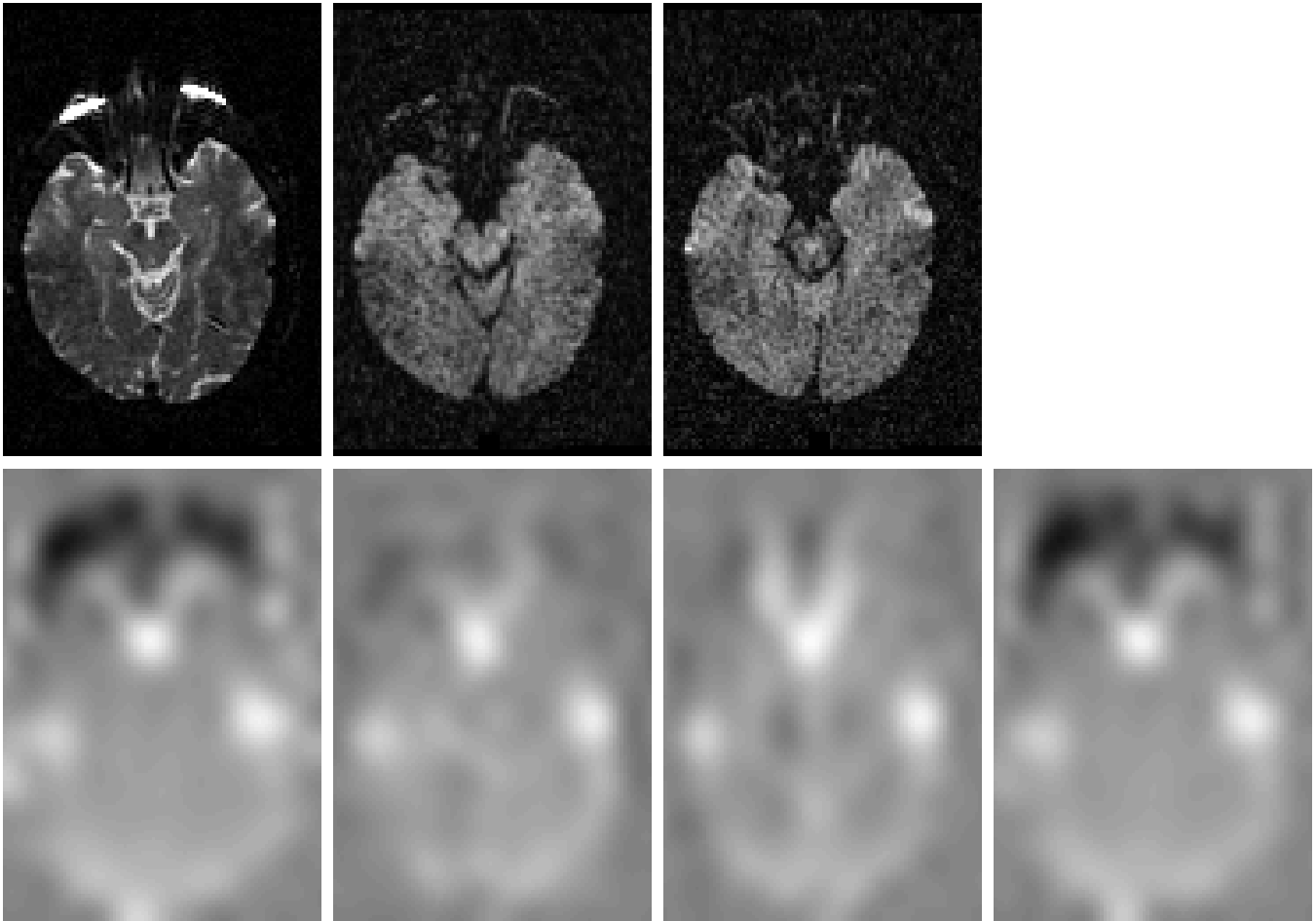


Fig. 8. The top row shows SE-EPI images acquired with positive phase-encode blips without diffusion gradients and with diffusion gradient directions $[0.17 \ 0.99 \ 0]$ and $[0.09 \ 0.19 \ -0.98]$ from left to right, respectively. The bottom row shows the fields estimated from the pairs (with positive and negative blips) corresponding to the top row. The fourth panel in the bottom row shows the field estimated using all pairs above and Eq. (22).

Sensitivity of estimated field with respect to data

Fields estimated from a pair of T_2 -weighted reference images and from pairs of diffusion weighted images are shown in the first three columns of Fig. 8. The fourth column shows the field resulting from using all three pairs and Eq. (22). There is a high degree of correspondence between the estimates. The main difference lies in the inability to estimate the field correctly around the eyes from the diffusion-weighted images. This is not surprising since the diffusion gradient obliterates virtually all the signal in the area. Note also how the field estimated from all three pairs is closest to that estimated from the reference pair. This is due to the much higher SNR of the T_2 -weighted scans, causing it to dominate any company as defined by Eq. (22).

Comparison to dual-echo phase mapping

Field maps obtained from the GE dual echo-time data and from dual-blip data using Eq. (21) are alternated in the second row of Fig. 9. Good correspondence is found between the two ways of estimating the fields. The final row

shows images restored using field map methods (the left in each pair) and the present method. A good correspondence can be seen also here.

Visual assessment of registration accuracy

One example of points defined in the anatomical image transferred to an uncorrected and a restored EPI image is shown in Fig. 10. It is evident that geometric fidelity has been much improved. Similar results were obtained for other image planes.

Generation of distortion-free diffusion tensor maps

The DT maps based on the undistorted EPI images are shown in Fig. 11 and showed (not surprisingly) the same apparent improvement in geometric fidelity as that evident in Fig. 10. The reason we show them is that it might be of interest to see the final maps resulting from a pair-wise restoration of all component images, rather than just a single pair.

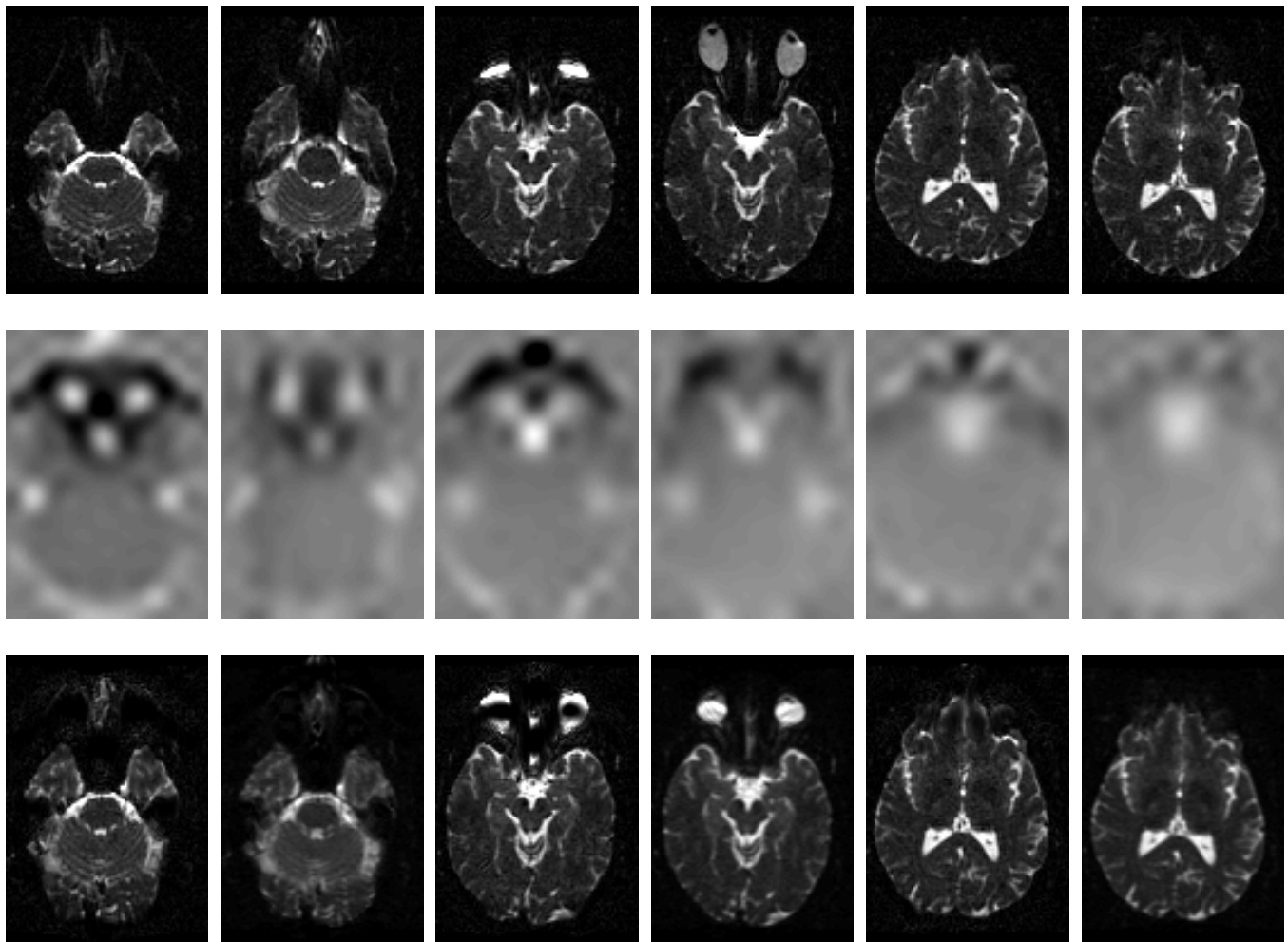


Fig. 9. The top panels show SE-EPI images acquired with positive (left in each pair) and negative (right in each pair) phase-encode blips for three different planes. The middle panels show the displacement-fields resulting from a direct measurement of the field using dual echo-times (left in each pair, see main text for details) and that estimated from the dual-blip data and the approximate model (right in each pair, Eqs. (18) to (21)). There is clearly a high degree of correspondence. The bottom row finally shows the restored images. In each pair, the left image was corrected using the measured field and Jacobian modulation and the right was restored using Eq. (10) and the estimated field.

Discussion

Diffusion tensor images based on SE-EPI images are subject to severe intensity and geometric distortions. Consider the pair of images in the top panel of Fig. 4, that these are from the same subject, both wrong, and that in a typical study you get one of them. It is then very intuitive that this is not ideal and that the problem should be properly addressed.

We have shown that, and explained why, it is not possible to reconstruct the true image from a single EPI acquisition, even with perfect knowledge of the field inhomogeneity $\Delta B_0(x, y, z)$. There is an inevitable, and irreversible, undersampling of the signal from areas where the susceptibility-induced local gradient collaborates with the phase-encode gradient of the sequence. This explains, for example, the observations made by Munger et al (2000). If not taken into consideration, i.e.,

if attempting a restoration based on a single EPI image, this will lead to a nonstationary image resolution. In particular for modern high field scanners this nonstationarity may be quite substantial.

We have suggested a solution to this problem based on revisiting an old idea (Bowtell et al., 1994) of acquiring two images, differing by a sign reversal of the phase-encode blips. This means that for each area where the local field and phase-encode gradients concur in one image they will oppose in the other, leading to an oversampling of the signal. This enables us to solve for the true intensity on a stationary grid in a least squares sense. In addition, we suggest a novel method to assess the field based exclusively on these two images, eliminating the need for any additional measurements (e.g., dual echo-time). In contrast to earlier methods (Bowtell et al., 1994; Kannengiesser et al., 1999) we estimate a true 3D field, simultaneously considering all the data, rendering it quite robust. On

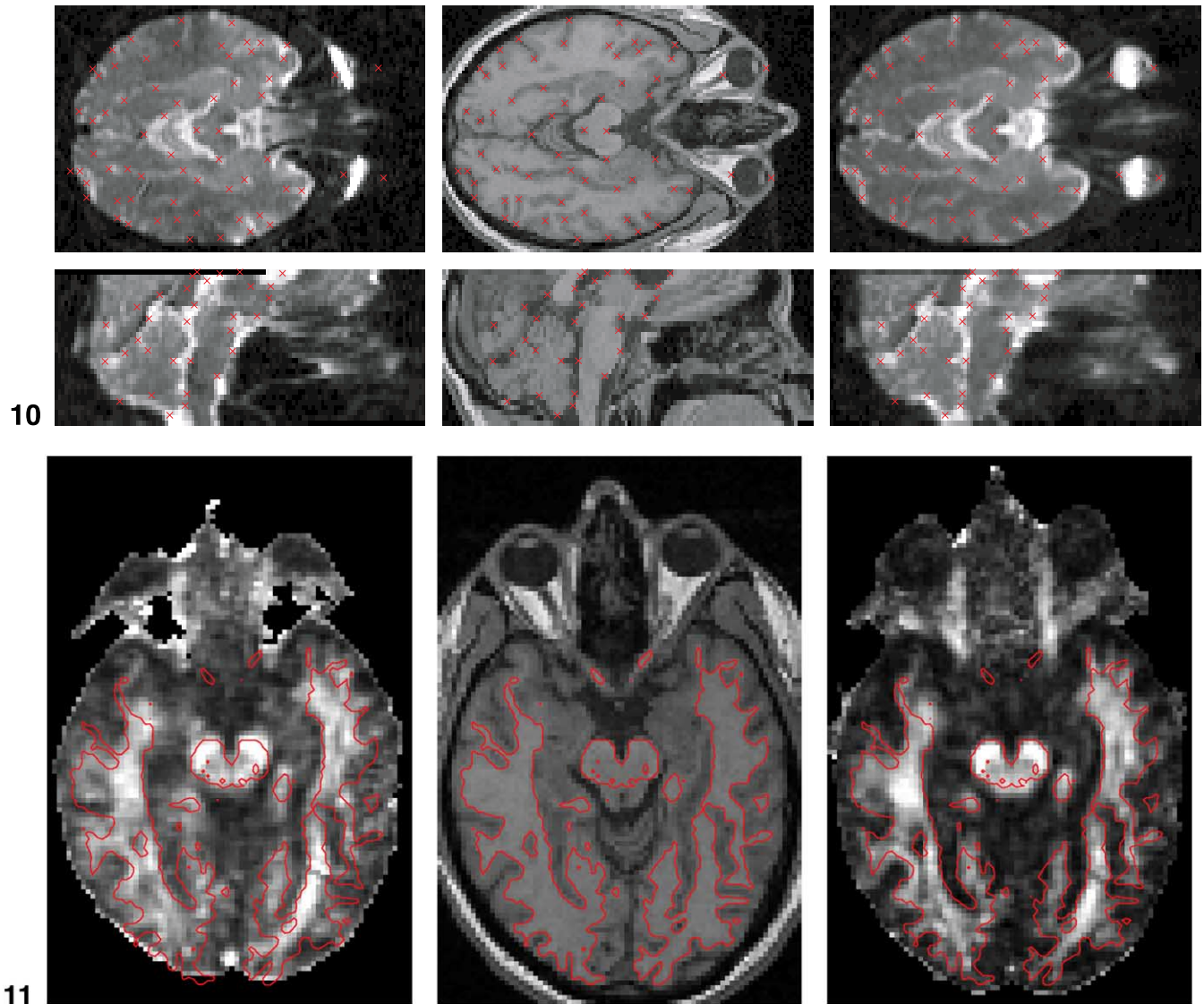


Fig. 10. An SE-EPI image with positive phase-encode blips (left) and an SE-EPI restored using a field estimated from dual-blip data (right) were coregistered to a T1-weighted 3D SPGR image. Points were manually defined on the SPGR image in sulci and in other readily identifiable locations. These were displayed in red on the SPGR image and in the coregistered SE-EPI images alike. It should be obvious from the images that the geometric fidelity has been vastly improved by the restoration approach.

Fig. 11. The same transversal SPGR slice that was shown in Fig. 10 is shown in the middle panel along with an isocontour serving as a crude delineation between white and gray matter. On the left is an anisotropy (FA) map based on bottom-up acquired SE-EPIs and on the right a map based on images restored from both acquisition directions. It is quite difficult to visually identify homologous structures between an anatomical scan and an anisotropy map. Still, the impression from Fig. 10 of a much higher geometric fidelity in the corrected image remains.

the downside it implies simultaneously estimating a large (several thousands) number of unknowns using an iterative procedure. This is potentially very time-consuming and prompted us to develop an approximate method that capitalises on a previously described method (Ashburner and Friston, 1999) that utilises the separability of the basis functions to speed up calculation of the curvature matrix.

The main equation of the paper is Eq. (22), which describes the updating rule for estimating the parameters from an entire DT data set. Compared to Eq. (21) that considers a single image pair, the execution time scales with the number of pairs. While we believe Eq. (22) to be important,

because it is principled way of utilising all data and because it points forward to future work, it appears to be “over the top” for the present application. It is our experience that using Eq. (21) with a T2-weighted reference pair, or with a pair consisting of the averages of all acquisitions for each k -space traversal direction, yields virtually identical results to using Eq. (22) with the entire data set (see, e.g., Fig. 8). Hence, we believe that in practice Eq. (21) will be used for the estimation of the field, followed by a pair-wise restoration of the images using the estimated field and Eq. (10). The execution time thus saved can be put to better use by including the largest possible number of basis functions

since it appears clear that a portion of these effects reside at rather high spatial frequencies (Fig. 6).

In addition to enabling a complete restoration of the images, we believe that our method offers advantages even when strictly considering just the evaluation of a field-map. As easy as it is in principle to calculate the field from a dual echo-time measurement (Jezzard and Balaban, 1995), as difficult is it in practice (see, e.g., Cusack and Papadakis, 2002). The need to unwrap the phase makes the problem highly nonlinear, involving a binary decision for each voxel. Inevitably, this leads to methods based on arbitrary heuristics (e.g., level of smoothing prior to unwrapping, part of volume to unwrap, temporal evolution of unwrapping, and basis set to fit to unwrapped map). It is certainly our experience that it is not easy to find a set of parameters that work satisfactorily for all data sets.

The method suggested by us is also nonlinear, but is based on an iterative sequence of linearisations of the problem. As such it appears to be quite robust for the range of distortions normally encountered in EPIs. Hence, we believe that the method can be an attractive alternative in any application where a field-map is desired.

An interesting option would be to use DT images to estimate high-resolution intersubject deformation fields. Previous attempts have been based on scalar anatomical data (e.g., Christensen et al., 1996; Ashburner et al., 1999) which means the all the information is contained along edges of different tissue types. This leads to solutions (deformation fields) that have a high frequency content along these edges and which are maximally smooth in between where there is effectively no information (see, e.g., Freeborough and Fox, 1998, for an illustrative example). This means that any local tissue loss in white matter will be attributed to a large, possibly global area.

By basing the estimation of the deformation fields on DT images (see, e.g., Alexander et al., 1999) white matter ceases to be a featureless lump and will now contain information that may be used to determine the local “deformations.” Hence, these deformation fields may prove useful for assessing temporal evolution or group differences in shape at a high resolution. An obvious prerequisite for this is that the images are anatomically faithful to begin with. We hope that the method suggested here might help provide that.

For gradient-echo EPI data (i.e., fMRI) the pristine image cannot be completely recovered in the manner described here. This is due to additional signal loss from “through plane” dephasing (Frahm et al., 1995). This is dephasing caused by susceptibility-induced field gradients orthogonal to the imaging plane and which is hence not rephased by the readout gradients. In spin-echo EPI the rephasing is accomplished by the 180° pulse (at least for the centre of k -space). In contrast, in gradient-echo EPI it leads to signal dropout (i.e., the signal is never measured and hence cannot be recovered by any amount of postprocessing).

However, the signal dropout will be independent of k -space acquisition direction so Eq. (15) should remain valid, allowing us to still use the approximate method to estimate the field. Hence, it might be of interest as an alternative to

dual echo-time measurements for finding either the “static” field map (Jezzard and Balaban, 1995) or the temporal (due to subject movement) development of the field (Hutton et al., 2002). The advantage over dual echo-times would be that both acquisitions are contributing to the signal-to-noise ratio of the time series in a straightforward manner.

High geometric fidelity would be especially important for studies where high-resolution fMRI data are collected and results projected onto flat-maps or reconstructed brain surfaces.

The application to fMRI data has not been examined in the present paper and will be the subject of future work.

Conclusion

We have described, implemented, and demonstrated a method for correction of susceptibility-induced geometrical and intensity distortions in EPI images. We have shown its usefulness for diffusion tensor images based on spin-echo EPI data. Furthermore, we believe it will prove useful also for gradient-echo EPI data used in fMRI.

Appendix:

Deriving the operational equations for the approximate method

In our implementation we use an $\mathbb{R}^3 \rightarrow \mathbb{R}^3$ mapping of the form $(x, y, z) = (u, v + d(u, v, w), w)$ (where (u, v, w) denotes the true undistorted space). From the perspective of a single voxel the intensity that rightfully belongs to that voxel is deflected by an equal distance in the bottom-up and the top-down acquired image. Hence, if we denote the two mappings T_+ and T_- for bottom-up and top-down, respectively, these are given by

$$(x, y, z)_+ = T_+(u, v, w) = (u, v - d(u, v, w), w) \quad (A1)$$

and

$$(x, y, z)_- = T_-(u, v, w) = (u, v + d(u, v, w), w), \quad (A2)$$

where the sign of the deflection has been arbitrarily chosen. If we use $f^*(u, v, w)$ to denote the undistorted intensity values in the undistorted space (“the truth”), we can describe the “restored” intensity function in two ways:

$$\begin{aligned} f^*(u, v, w) &= \left(1 - \frac{\partial d}{\partial v}\right) f_+(u, v - d(u, v, w), w) \\ &= \left(1 + \frac{\partial d}{\partial v}\right) f_-(u, v + d(u, v, w), w). \end{aligned} \quad (A3)$$

Of these, we will use the second equality where f_+ and f_- are our observed data and the d -field is the unknown of our problem.

Up until now we have treated the problem as a continuous one, when in reality we have sampled f_+ and f_- (and hence also d) on a discrete grid. In fact, f_+ and f_- have been sampled on two distinct grids. If we assume integers a , b , and c , these are given by $(u_0 + a\Delta u, v_0 + b\Delta v - d(u + a\Delta u, v + b\Delta v, w + c\Delta w), w + c\Delta w)$ and $(u_0 + a\Delta u, v_0 + b\Delta v + d(u + a\Delta u, v + b\Delta v, w + c\Delta w), w + c\Delta w)$, respectively. It is when we consider the discrete version of the problem that Eq. (A3) above becomes an approximation, which is why we refer to it as the “approximate method.” For the discrete case, we will denote the acquired data by \mathbf{f}_+ and \mathbf{f}_- , being $n \times 1$ column vectors obtained by unravelling an image volume into a single “thread.” The displacement field is modelled as a linear combination of basis warps, i.e.,

$$\underbrace{\mathbf{d}}_{n \times 1} = \underbrace{[\mathbf{B}_1 \quad \mathbf{B}_2 \quad \cdots \quad \mathbf{B}_{m_x m_y m_z}]}_{n \times m_x m_y m_z} \underbrace{\mathbf{b}}_{m_x m_y m_z \times 1} = \mathbf{B}\mathbf{b}, \quad (\text{A4})$$

where each vector \mathbf{B}_i is an unravelled version of one basis function from a truncated 3D discrete cosine transform and where m_x , m_y , and m_z are the order of the transform in the x -, y -, and z -directions, respectively. Furthermore, given that we have measured \mathbf{f}_+ (or \mathbf{f}_-) on some grid we can estimate the value for an arbitrary point in the volume using interpolation (trilinear or sinc). When we have a nonzero \mathbf{b} vector (and hence a nonzero displacement field \mathbf{d}) we will sample (by interpolation and Jacobian intensity modulation) new points, yielding a new vector of values. We will denote this resampled and modulated vector $\mathbf{f}_+(\mathbf{b})$ (or $\mathbf{f}_-(\mathbf{b})$ for the top-down data). Hence, we view \mathbf{f}_+ (or \mathbf{f}_-) as a continuous n -dimensional function of $m_x \times m_y \times m_z$ variables (i.e., a $\mathbb{R}^{m_x m_y m_z} \rightarrow \mathbb{R}^n$ mapping). The objective function that we wish to minimise in order to find \mathbf{b} is simply the sum of squared differences between $\mathbf{f}_+(\mathbf{b})$ and $\mathbf{f}_-(\mathbf{b})$ (i.e., $O(\mathbf{b}) = (\mathbf{f}_+(\mathbf{b}) - \mathbf{f}_-(\mathbf{b}))^T(\mathbf{f}_+(\mathbf{b}) - \mathbf{f}_-(\mathbf{b}))$).

As we alluded to in the main text, there is another potential cause of differences between \mathbf{f}_+ and \mathbf{f}_- , namely subject movements between the two acquisitions. If we denote the six parameters associated with a rigid body model by \mathbf{p} we can denote the resampled vector \mathbf{f}_+ that is obtain after transforming the sampling points first with a rigid body model according to \mathbf{p} and then a displacement field according to \mathbf{b} by $\mathbf{f}_+(\mathbf{p}, \mathbf{b})$. We could pick any of the acquisitions as reference, in terms of subject position, but have instead opted for realignment to the geometrical midpoint, thereby rendering both \mathbf{f}_+ and \mathbf{f}_- functions of both \mathbf{p} and \mathbf{b} . In the following we will use the “residual error” formulation (Andersson and Skare, 2002) when deriving the equations because it is more convenient

when extending the model to include more than just a single pair of images. From Eq. (A3) the model for a single voxel is

$$\begin{bmatrix} f_+(\mathbf{p}, \mathbf{b}) \\ f_-(\mathbf{p}, \mathbf{b}) \end{bmatrix} = \begin{bmatrix} 1 \\ 1 \end{bmatrix} \boldsymbol{\mu} + \begin{bmatrix} e_+ \\ e_- \end{bmatrix}, \quad (\text{A5})$$

yielding the residual forming matrix

$$\mathbf{R} = \frac{1}{2} \begin{bmatrix} 1 & -1 \\ -1 & 1 \end{bmatrix} \quad (\text{A6})$$

and extending the model to all voxels

$$\underbrace{\mathbf{R}}_{2n \times 2n} = \frac{1}{2} \begin{bmatrix} \underbrace{\mathbf{I}}_{n \times n} & \underbrace{-\mathbf{I}}_{n \times n} \\ \underbrace{-\mathbf{I}}_{n \times n} & \underbrace{\mathbf{I}}_{n \times n} \end{bmatrix}, \quad (\text{A7})$$

which makes the objective function

$$\begin{aligned} O(\mathbf{p}, \mathbf{b}) &= \frac{1}{2} [\mathbf{f}_+(\mathbf{p}, \mathbf{b})^T \quad \mathbf{f}_-(\mathbf{p}, \mathbf{b})^T] \\ &\quad \times \begin{bmatrix} \mathbf{I} & -\mathbf{I} \\ -\mathbf{I} & \mathbf{I} \end{bmatrix} \begin{bmatrix} \mathbf{f}_+(\mathbf{p}, \mathbf{b}) \\ \mathbf{f}_-(\mathbf{p}, \mathbf{b}) \end{bmatrix}. \end{aligned} \quad (\text{A8})$$

As demonstrated by Andersson and Skare (2002) this results in the following update rule for a Levenberg–Marquardt type algorithm for minimisation of $O(\mathbf{p}, \mathbf{b})$,

$$\begin{aligned} &\underbrace{\begin{bmatrix} \mathbf{p}_{i+1} - \mathbf{p}_i \\ \mathbf{b}_{i+1} - \mathbf{b}_i \end{bmatrix}}_{6 + m_x m_y m_z \times 1} \\ &= - \left(\begin{bmatrix} \underbrace{\left(\frac{\partial \mathbf{f}}{\partial \mathbf{p}} \right)^T}_{6 \times 2n} \\ \underbrace{\left(\frac{\partial \mathbf{f}}{\partial \mathbf{b}} \right)^T}_{m_x m_y m_z \times 2n} \end{bmatrix} \underbrace{\begin{bmatrix} \mathbf{I} & -\mathbf{I} \\ -\mathbf{I} & \mathbf{I} \end{bmatrix}}_{2n \times 2n} \underbrace{\begin{bmatrix} \left(\frac{\partial \mathbf{f}}{\partial \mathbf{p}} \right) \\ \left(\frac{\partial \mathbf{f}}{\partial \mathbf{b}} \right) \end{bmatrix}}_{\substack{2n \times 6 \\ 2n \times m_x m_y m_z}} \right)^{-1} \\ &\quad \times \begin{bmatrix} \underbrace{\left(\frac{\partial \mathbf{f}}{\partial \mathbf{p}} \right)^T}_{6 \times 2n} \\ \underbrace{\left(\frac{\partial \mathbf{f}}{\partial \mathbf{b}} \right)^T}_{m_x m_y m_z \times 2n} \end{bmatrix} \underbrace{\begin{bmatrix} \mathbf{I} & -\mathbf{I} \\ -\mathbf{I} & \mathbf{I} \end{bmatrix}}_{2n \times 2n} \underbrace{\begin{bmatrix} \mathbf{f}_+(\mathbf{p}, \mathbf{b}) \\ \mathbf{f}_-(\mathbf{p}, \mathbf{b}) \end{bmatrix}}_{2n \times 1}, \end{aligned} \quad (\text{A9})$$

where

$$\frac{\partial \mathbf{f}}{\partial \mathbf{p}} = \begin{bmatrix} \frac{\partial \mathbf{f}_+}{\partial \mathbf{p}} \\ \frac{\partial \mathbf{f}_-}{\partial \mathbf{p}} \end{bmatrix} \quad (\text{A10})$$

and

$$\frac{\partial \mathbf{f}}{\partial \mathbf{b}} = \begin{bmatrix} \frac{\partial \mathbf{f}_+}{\partial \mathbf{b}} \\ \frac{\partial \mathbf{f}_-}{\partial \mathbf{b}} \end{bmatrix}. \quad (\text{A11})$$

Given Eq. (A3) and (A4) above we can describe the partial derivatives with respect to \mathbf{b} as

$$\frac{\partial \mathbf{f}_+}{\partial \mathbf{b}} = -\underbrace{\text{diag}\left(\frac{\partial \mathbf{f}_+}{\partial \mathbf{y}}\right)}_{n \times n} \underbrace{\mathbf{B}}_{n \times m} - \underbrace{\text{diag}(\mathbf{f}_+)}_{n \times n} \underbrace{\frac{\partial \mathbf{B}}{\partial \mathbf{y}}}_{n \times m}, \quad (\text{A12})$$

and

$$\frac{\partial \mathbf{f}_-}{\partial \mathbf{b}} = +\underbrace{\text{diag}\left(\frac{\partial \mathbf{f}_-}{\partial \mathbf{y}}\right)}_{n \times n} \underbrace{\mathbf{B}}_{n \times m} + \underbrace{\text{diag}(\mathbf{f}_-)}_{n \times n} \underbrace{\frac{\partial \mathbf{B}}{\partial \mathbf{y}}}_{n \times m}, \quad (\text{A13})$$

where $m = m_x m_y m_z$ and where, given an $n \times 1$ vector \mathbf{a} , the *diag* operator creates an $n \times n$ matrix with the values of \mathbf{a} on the diagonal.

Implementation of Eq. (A9) requires some care since it involves the multiplication of some really large matrices. Specifically we define the matrix \mathbf{A} as

$$\mathbf{A} = \begin{bmatrix} \left[\begin{array}{c} \left(\frac{\partial \mathbf{f}_+}{\partial \mathbf{p}} \right)^T \left(\frac{\partial \mathbf{f}_-}{\partial \mathbf{p}} \right)^T \\ \underbrace{\mathbf{B}^T}_{m \times n} \left[\underbrace{-\text{diag}\left(\frac{\partial \mathbf{f}_+}{\partial \mathbf{y}}\right)}_{n \times 2n} \quad \underbrace{\text{diag}\left(\frac{\partial \mathbf{f}_-}{\partial \mathbf{y}}\right)}_{n \times 2n} \right] + \underbrace{\left(\frac{\partial \mathbf{B}}{\partial \mathbf{y}}\right)^T}_{m \times n} \left[\underbrace{-\text{diag}(\mathbf{f}_+)}_{n \times 2n} \quad \underbrace{\text{diag}(\mathbf{f}_-)}_{n \times 2n} \right] \end{array} \right] \begin{bmatrix} \mathbf{I} & -\mathbf{I} \\ -\mathbf{I} & \mathbf{I} \end{bmatrix} \\ \underbrace{\left[\begin{array}{c} \frac{\partial \mathbf{f}_+}{\partial \mathbf{p}} \\ \frac{\partial \mathbf{f}_-}{\partial \mathbf{p}} \end{array} \right]}_{2n \times 6} \underbrace{\left[\begin{array}{c} -\text{diag}\left(\frac{\partial \mathbf{f}_+}{\partial \mathbf{y}}\right) \\ \text{diag}\left(\frac{\partial \mathbf{f}_-}{\partial \mathbf{y}}\right) \end{array} \right]}_{2n \times n} \underbrace{\mathbf{B}}_{n \times m} + \underbrace{\left[\begin{array}{c} -\text{diag}(\partial \mathbf{f}_+) \\ \text{diag}(\partial \mathbf{f}_-) \end{array} \right]}_{2n \times n} \underbrace{\frac{\partial \mathbf{B}}{\partial \mathbf{y}}}_{n \times m} \end{bmatrix}. \quad (\text{A14})$$

The direct creation of \mathbf{A} would entail calculating roughly $m^2/2$ elements, each requiring $2n$ multiplications and additions. With m in the order of thousands (which is demonstrated to be needed in the main text) and n in the order of hundreds of thousands this is a formidable task even for present day computers. Luckily, we are able to use the cunning trick suggested by Ashburner and Friston (1999) where they capitalise on the fact that \mathbf{B} is separable into a Kronecker product, i.e., $\mathbf{B} = \mathbf{B}_z \otimes \mathbf{B}_y \otimes \mathbf{B}_x$. When a matrix \mathbf{B} is separable in that way $\mathbf{B}^T \mathbf{B}$ can be calculated as $\mathbf{B}^T \mathbf{B} = \mathbf{B}_z^T \mathbf{B}_z \otimes \mathbf{B}_y^T \mathbf{B}_y \otimes \mathbf{B}_x^T \mathbf{B}_x$, which is ridiculously fast compared to the direct calculation. What Ashburner and Friston (1999)

showed was that with some additional thought it is possible to find a similar shortcut for $(\mathbf{B}_z \otimes \mathbf{B}_y \otimes \mathbf{B}_x)^T \mathbf{D} \mathbf{D} (\mathbf{B}_z \otimes \mathbf{B}_y \otimes \mathbf{B}_x)$ where \mathbf{D} is some arbitrary diagonal matrix. In the present paper we will use also the fact (stated without proof) that there is a shortcut also for $(\mathbf{C}_z \otimes \mathbf{C}_y \otimes \mathbf{C}_x)^T \mathbf{D}_1 \mathbf{D}_2 (\mathbf{B}_z \otimes \mathbf{B}_y \otimes \mathbf{B}_x)$ where \mathbf{C} is a matrix implementing some other separable 3D basis set and where \mathbf{D}_1 and \mathbf{D}_2 are both diagonal matrices. We will refer to these as SC1 and SC2 (shortcut 1 and 2).

Some additional consideration of Eq. (A14) shows that it can be thought of as consisting of a small set of submatrices,

$$\mathbf{A} = \begin{bmatrix} \mathbf{X}_1^T \\ \mathbf{X}_2^T + \mathbf{X}_3^T \end{bmatrix} \mathbf{R} [\mathbf{X}_1 \quad \mathbf{X}_2 + \mathbf{X}_3] = \begin{bmatrix} \underbrace{\mathbf{X}_1^T \mathbf{R} \mathbf{X}_1}_{6 \times 6} & \underbrace{\mathbf{X}_1^T \mathbf{R} \mathbf{X}_2 + \mathbf{X}_1^T \mathbf{R} \mathbf{X}_3}_{6 \times m} \\ \underbrace{(\mathbf{X}_1^T \mathbf{R} \mathbf{X}_2 + \mathbf{X}_1^T \mathbf{R} \mathbf{X}_3)^T}_{m \times 6} & \underbrace{\mathbf{X}_2^T \mathbf{R} \mathbf{X}_2 + \mathbf{X}_3^T \mathbf{R} \mathbf{X}_3 + \mathbf{X}_2^T \mathbf{R} \mathbf{X}_3 + (\mathbf{X}_2^T \mathbf{R} \mathbf{X}_3)^T}_{m \times m} \end{bmatrix}, \quad (\text{A15})$$

where

$$\mathbf{R} = \begin{bmatrix} \mathbf{I} & -\mathbf{I} \\ -\mathbf{I} & \mathbf{I} \end{bmatrix} \quad (\text{A16})$$

and where the specifics of \mathbf{X}_1 , \mathbf{X}_2 , and \mathbf{X}_3 should be clear from a comparison to Eq. (A14).

Deriving these a bit further it is easy to see that

$$\mathbf{X}_1^T \mathbf{R} \mathbf{X}_1 = \begin{bmatrix} \frac{\partial \mathbf{f}_+}{\partial \mathbf{p}} + \frac{\partial \mathbf{f}_-}{\partial \mathbf{p}} \end{bmatrix}^T \begin{bmatrix} \frac{\partial \mathbf{f}_+}{\partial \mathbf{p}} + \frac{\partial \mathbf{f}_-}{\partial \mathbf{p}} \end{bmatrix}, \quad (\text{A17})$$

which does not take long to calculate directly. Furthermore,

$$\mathbf{X}_2^T \mathbf{R} \mathbf{X}_2 = \mathbf{B}^T \text{diag} \left(\frac{\partial \mathbf{f}_+}{\partial y} + \frac{\partial \mathbf{f}_-}{\partial y} \right) \text{diag} \left(\frac{\partial \mathbf{f}_+}{\partial y} + \frac{\partial \mathbf{f}_-}{\partial y} \right) \mathbf{B} \quad (\text{A18})$$

and

$$\mathbf{X}_3^T \mathbf{R} \mathbf{X}_3 = \left(\frac{\partial \mathbf{B}}{\partial y} \right)^T \text{diag}(\mathbf{f}_+ + \mathbf{f}_-) \text{diag}(\mathbf{f}_+ + \mathbf{f}_-) \frac{\partial \mathbf{B}}{\partial y}, \quad (\text{A19})$$

where

$$\frac{\partial \mathbf{B}}{\partial y} = \underbrace{\mathbf{B}_z}_{n_z \times m_z} \otimes \underbrace{\frac{\partial \mathbf{B}_y}{\partial y}}_{n_y \times m_y} \otimes \underbrace{\mathbf{B}_x}_{n_x \times m_x}, \quad (\text{A20})$$

i.e., separable, and where n_x , n_y , and n_z are the volume size (in voxels) in the x -, y -, and z -direction, respectively. It is clear that both of these are of a form suitable for SC1 and hence we can calculate them rapidly. The next term is given by

$$\mathbf{X}_2^T \mathbf{R} \mathbf{X}_3 = \left(\frac{\partial \mathbf{B}}{\partial y} \right)^T \text{diag}(\mathbf{f}_+ + \mathbf{f}_-) \text{diag} \left(\frac{\partial \mathbf{f}_+}{\partial y} + \frac{\partial \mathbf{f}_-}{\partial y} \right) \mathbf{B}, \quad (\text{A21})$$

which can be calculated using SC2, and the fourth term finally is just the transpose of the third term.

Ashburner and Friston (1999) also discuss the related problem of calculating $\mathbf{B}^T \mathbf{D} \mathbf{y}$, where \mathbf{y} is an $n \times 1$ column vector, and derive a shortcut also for this calculation. This we might call SC3. It is easily shown that

$$\underbrace{(\mathbf{X}_1^T \mathbf{R} \mathbf{X}_2)}_{m \times 6} = \underbrace{\mathbf{B}^T}_{m \times n} \underbrace{\text{diag} \left(\frac{\partial \mathbf{f}_+}{\partial y} + \frac{\partial \mathbf{f}_-}{\partial y} \right)}_{n \times n} \underbrace{\left(\frac{\partial \mathbf{f}_+}{\partial \mathbf{p}} + \frac{\partial \mathbf{f}_-}{\partial \mathbf{p}} \right)}_{n \times 6} \quad (\text{A22})$$

and

$$\underbrace{(\mathbf{X}_1^T \mathbf{R} \mathbf{X}_3)}_{m \times 6} = \underbrace{\left(\frac{\partial \mathbf{B}}{\partial y} \right)^T}_{m \times n} \underbrace{\text{diag}(\mathbf{f}_+ + \mathbf{f}_-)}_{n \times n} \underbrace{\left(\frac{\partial \mathbf{f}_+}{\partial \mathbf{p}} + \frac{\partial \mathbf{f}_-}{\partial \mathbf{p}} \right)}_{n \times 6}. \quad (\text{A23})$$

This formulation is relevant because it shows how the terms of the off-diagonal partitions in Eq. (A15) can be calculated by

six (one for each column of $(\frac{\partial \mathbf{f}_+}{\partial \mathbf{p}} + \frac{\partial \mathbf{f}_-}{\partial \mathbf{p}})$) consecutive calculations of the same type as $\mathbf{B}^T \mathbf{D} \mathbf{y}$. Hence, there is a rapid way of calculating these terms also.

That is really all there is to it. Combining Eq. (A9), (A14), (A15), (A17), (A18), (A19), (A21), (A22), and (A23) offers a fast and convenient way to estimate the field.

Acknowledgments

We gratefully acknowledge the financial support of the Swedish Research Council (Grant 621-2001-2844).

References

- Alexander, D.C., Gee, J.C., Bajcsy, R.K., 1999. Elastic matching of diffusion tensor MRI's. Proceedings of the Computer Vision and Pattern Recognition Conference, Los Alamitos, CA, pp. 313–318.
- Andersson, J.L.R., Hutton, C., Ashburner, J., Turner, R., Friston, K., 2001. Modelling geometric deformations in EPI time series. *NeuroImage* 13, 903–919, doi:10.1006/nimg.2001.0746.
- Andersson, J.L.R., Skare, S., 2002. A model-based method for retrospective correction of geometric distortions in diffusion-weighted EPI. *NeuroImage* 16, 177–199, doi:10.1006/nimg.2001.1039.
- Ashburner, J., Hutton, C., Frackowiak, R.S.J., Johnsrude, I., Price, C., Friston, K.J., 1998. Identifying global anatomical differences: deformation-based morphometry. *Hum. Brain Mapp.* 6, 348–357.
- Ashburner, J., Friston, K.J., 1999. Nonlinear spatial normalization using basis functions. *Hum. Brain Mapp.* 7, 254–266.
- Ashburner, J., Andersson, J.L.R., Friston, K.J., 1999. High-dimensional image registration using symmetric priors. *NeuroImage* 9, 619–628.
- Ashburner, J., Friston, K.J., 2000. Voxel-based morphometry—the methods. *NeuroImage* 11, 805–821.
- Basser, P.J., Mattiello, J., Le Bihan, D., 1994. Estimation of the effective self-diffusion tensor from the NMR spin echo. *J. Magn. Reson. B* 103, 247–254.
- Bowtell, R., McIntyre, D.J.O., Commandre, M.-J., Glover, P.M., Mansfield, P., 1994. Correction of geometric distortion in echo planar images. Proceedings of the 2nd Meeting of the Society of Magnetic Resonance, p. 411.
- Chang, H., Fitzpatrick, J.M., 1992. A technique for accurate magnetic resonance imaging in the presence of field inhomogeneities. *IEEE Trans. Med. Imaging* 11, 319–329.
- Christensen, G.E., Rabbitt, R.D., Miller, M.I., 1996. Deformable templates using large deformation kinematics. *IEEE Trans. Imaging Proc.* 5, 1435–1447.
- Cusack, R., Papadakis, N., 2002. New robust 3-D phase-unwrapping algorithms: application to magnetic field-mapping and undistorting echoplanar images. *NeuroImage* 16, 754–764, doi:10.1006/nimg.2002.1092.
- Frahm, J., Merboldt, K.-D., Hänicke, W., 1995. The effects of intravoxel dephasing and incomplete slice refocusing on susceptibility contrast in gradient-echo MRI. *J. Magn. Reson. B* 109, 234–237.
- Freeborough, P.A., Fox, N.C., 1998. Modelling brain deformations in Alzheimer disease by fluid registration of serial 3D MR images. *J. Comput. Assist. Tomogr.* 22, 838–843.
- Gaser, C., Volz, H.P., Kiebel, S., Riehemann, S., Sauer, H., 1999. Detecting structural changes in whole brain based on nonlinear deformations—application to schizophrenia research. *NeuroImage* 10, 107–113.
- Good, C.D., Johnsrude, I.S., Ashburner, J., Henson, R.N.A., Friston, K.J., Frackowiak, R.S.J., 2001. A voxel-based morphometric study of ageing in 465 normal adult human brains. *NeuroImage* 14, 21–36, doi: 10.1006/nimg.2001.0786.

- Gudbjartsson, H., Maier, S.E., Mulkern, R.V., Morocz, I.A., Patz, S., Jolesz, F.A., 1996. Line scan diffusion imaging. *Magn. Reson. Med.* 36, 509–519.
- Hutton, C., Bork, A., Josephs, O., Deichmann, R., Ashburner, J., Turner, R., 2002. Image distortion correction in fMRI: a quantitative evaluation. *NeuroImage* 16, 217–240, doi:10.1006/nimg.2001.1054.
- Jain, A.K., 1989. *Fundamentals of Digital Image Processing*. Prentice-Hall, New Jersey.
- Jenkinson, M., 2001. Improved unwarping of EPI images using regularised B0 maps. *NeuroImage* 13, S165.
- Jenkinson, M., 2003. Fast, automated, N-dimensional phase-unwrapping algorithm. *Magn. Reson. Med.* 49, 193–197.
- Jezzard, P., Balaban, R.S., 1995. Correction for geometric distortion in echo-planar images from B₀ field variations. *Magn. Reson. Med.* 34, 65–73.
- Jezzard, P., Barnett, A.S., Pierpaoli, C., 1998. Characterisation of and correction for eddy current artefacts in echo planar diffusion imaging. *Magn. Reson. Med.* 39, 801–812.
- Jones, D.K., Horsfield, M.A., Simmons, A., 1999. Optimal strategies for measuring diffusion in anisotropic systems by magnetic resonance imaging. *Magn. Reson. Med.* 42, 515–525.
- Kadah, Y.M., Hu, X., 1997. Simulated phase evolution rewinding (sphere): a technique for reducing B0 inhomogeneity effects in MR images. *Magn. Reson. Med.* 38, 615–627.
- Kannengiesser, S.A.R., Wang, Y., Haacke, E.M., 1999. Geometric distortion correction in gradient-echo imaging by use of dynamic time warping. *Magn. Reson. Med.* 42, 585–590.
- Kybic, J., Thévenaz, P., Nirkko, A., Unser, M., 2000. Unwarping of unidirectionally distorted EPI images. *IEEE Trans. Med. Imaging* 19, 80–93.
- Le Bihan, D., Breton, E., Lallemand, D., Grenier, P., Cabanis, E., Laval-Jeantet, M., 1986. MR imaging of intravoxel incoherent motions: application to diffusion and perfusion in neurologic disorders. *Radiology* 161, 401–407.
- Maes, F., Collignon, A., Vandermeulen, D., Marchal, G., Suetens, P., 1997. Multimodality image registration by maximisation of mutual information. *IEEE Trans. Med. Imaging* 16, 187–198.
- Maguire, E.A., Gadian, D.G., Johnsrude, I.S., Good, C.D., Ashburner, J., Frackowiak, R.S.J., Frith, C.D., 2000. Navigation-related structural changes in the hippocampi of taxi drivers. *Proc. Natl. Acad. Sci. USA* 97, 4398–4403.
- Marsden, J.E., Tromba, A.J., 1981. *Vector Calculus*, 2nd ed. Freeman, San Francisco.
- May, A., Ashburner, J., Buchel, C., McGonigle, D.J., Friston, K.J., Frackowiak, R.S.J., Goadsby, P.J., 1999. Correlation between structural and functional changes in brain in an idiopathic headache syndrome. *Nat. Med.* 5, 836–838.
- Munger, P., Crelier, G.R., Peters, T.M., Pike, G.B., 2000. An inverse problem approach to the correction of distortion in EPI images. *IEEE Trans. Med. Imaging* 19, 681–689.
- Pierpaoli, C., Jezzard, P., Basser, P.J., Barnett, A., Di Chiro, G., 1996. Diffusion tensor MR imaging of the human brain. *Radiology* 201, 637–648.
- Powell, M.J.D., 1964. An efficient method for finding the minimum of several variables without calculating derivatives. *Comput. J.* 7, 155–163.
- Skare, S., Hedehus, M., Moseley, M.E., Li, T.-Q., 2000. Condition number as a measure of noise performance of diffusion tensor data acquisition schemes with MRI. *J. Magn. Reson.* 147, 340–352.
- Skare, S., Andersson, J.L.R., 2001. On the effects of gating in diffusion imaging of the brain using single shot EPI. *Magn. Reson. Imaging* 19, 1125–1128.
- Studholme, C., Constable, R.T., Duncan, J.S., 2000. Accurate alignment of functional EPI data to anatomical MRI using a physics-based distortion model. *IEEE Trans. Med. Imag.* 19, 1115–1127.
- Thurfjell, L., Bohm, C., Greitz, T., Eriksson, L., 1993. Transformations and algorithms in a computerized brain atlas. *IEEE Trans. Nucl. Sci.* 40, 1187–1191.
- Turner, R., Le Bihan, D., Maier, J., Vavrek, R., Hedges, L.K., Pekar, J., 1990. Echo-planar imaging of intra-voxel incoherent motion. *Radiology* 177, 407–414.
- Weis, J., Budinsky, L., 1990. Simulation of the influence of magnetic field inhomogeneity and distortion correction in MR imaging. *Magn. Reson. Imaging* 8, 483–489.
- Woods, R.P., Grafton, S.T., Watson, J.D.G., Sicotte, N.L., Mazziotta, J.C., 1998. Automated image registration: II. Intersubject validation of linear and nonlinear models. *J. Comput. Assist. Tomogr.* 22 (1), 153–165.
- Wright, I.C., McGuire, P.K., Poline, J.-B., Traverso, J.M., Murray, C.D., Frith, C.D., Frackowiak, R.S.J., Friston, K.J., 1995. A voxel-based method for the statistical analysis of gray and white matter density applied to schizophrenia. *NeuroImage* 2, 244–252.